Resiliency-Oriented Operation of Distribution Networks under Unexpected Wildfires Using Multi-Horizon Information-Gap Decision Theory

Mehdi Izadi [a], Seyed Hossein Hosseinian [b], Shahab Dehghan [c, *], Ahmad Fakharian [a], Nima Amjady [d]

[a] Faculty of Electrical, Biomedical, and Mechatronics Engineering, Qazvin Branch, Islamic Azad University, Qazvin, Iran.
[b] Department of Electrical Engineering, Amirkabir University of Technology, Tehran, Iran.
[c] School of Engineering, Newcastle University, Newcastle upon Tyne, UK.
[d] Center for New Energy Transition Research (CfNETR), Federation University, Ballarat, Australia.

Abstract

Extreme events may trigger cascading outages of different components in power systems and cause a substantial loss of load. Forest wildfires, as a common type of extreme events, may damage transmission/distribution lines across the forest and disconnect a large number of consumers from the electric network. Hence, this paper presents a robust scheduling model based on the notion of information-gap decision theory (IGDT) to enhance the resilience of a distribution network exposed to wildfires. Since the thermal rating of a transmission/distribution line is a function of its temperature and current, it is assumed that the tie-line connecting the distribution network to the main grid is equipped with a dynamic thermal rating (DTR) system aiming at accurately evaluating the impact of a wildfire on the ampacity of the tie-line. The proposed approach as a multi-horizon IGDT-based optimization problem finds a robust operation plan protected against the uncertainty of wind power, solar power, load, and ampacity of tie-lines under a specific uncertainty budget (*UB*). Since all uncertain parameters compete to maximize their robust regions under a specific uncertainty budget, the proposed multi-horizon IGDT-based model is solved by the augmented normalized normal constraint (ANNC) method as an effective multi-objective optimization approach. Moreover, a posteriori out-of-sample analysis is used to find (i) the best solution among the set of Pareto optimal solutions obtained from the ANNC method given a specific uncertainty budget, and (ii) the best resiliency level by varying the uncertainty budget and finding the optimal uncertainty budget. The proposed approach is tested on a 33-bus distribution network under different circumstances. The case study under different conditions verifies the effectiveness of the proposed operation planning model to enhance the resilience of a distribution network under a close wildfire.

Keywords: Distribution Network Resilient Operation (DNRO), Dynamic Thermal Rating (DTR), Information Gap-Decision Theory (IGDT), Wildfire.

Nomenclature

A. Acronyms

AC	Alternative Current
ACSR	Aluminum Conductor Steel-Reinforced
ANNC	Augmented Normalized Normal Constraint
DER	Distributed Energy Resources
DNRO	Distribution Network Resilient Operation
DR	Demand Response
DSO	Distribution System Operator
DTR	Dynamic Thermal Rating
ESS	Energy Storage System
IGDT	Information Gap-Decision Theory
MISOCP	Mixed-Integer Second-Order Conic Programming
MOMP	Multi-Objective Mathematical Programming
MT	Micro Turbine
MUFS	Model of Urban Fire Spread
NNC	Normalized Normal Constraint
OPF	Optimal Power Flow

* Corresponding author (email: shahab.dehghan@newcastle.ac.uk)

PMT	Portable Micro Turbine
PV	Photovoltaic panel
SOCP	Second-Order Conic Programming
WT	Wind Turbine

B. Functions

$\mathcal{F}_k(\vartheta)$	The kth objective function of the MOMP problem.
$\mathcal{F}_k^n(\vartheta)$	The kth normalized objective function of the MOMP problem.
$\mathcal{F}_k^{bst}(\vartheta_k^{bst})$	Best value in the kth column of the payoff matrix (i.e., optimal value of the kth objective function).
$\mathcal{F}_k^{wst}(\vartheta_k^{bst})$	Worst value of the kth column in the payoff matrix.
OF	Objective function.

C. Indices, Sets, and Symbols

ij	Index of line connecting buses i and j.
h, i, j	Index of buses (1 to N^B).
k, z	Index of objective functions in MOMP (1 to m).
l	Index of utopia hyper-plane points (or division points).
lk	Index of weighting parameter related to l^{th} utopia hyper-plane point and k^{th} objective function in MOMP.
s	Index of scenario vectors (1 to N^S).
t, τ	Index of hours (1 to N^T).
u	Index of each member of Ω^{UB}.
$\Gamma^\bullet$	Robust region of the uncertainty source $\bullet$.
Ξ^D	Feasible space of the D-DNRO model.
Ξ^{IGDT}	Feasible space of the IGDT-DNRO problem.
Ξ^{MOMP}	Feasible space of the MOMP problem.
Ω^{UB}	Set of allowed values for the budget of uncertainty.
$\|\bullet\|$	Magnitude of variable $\bullet$.
$\|\bullet\|$	Euclidian norm of vector $\bullet$.
$\overline{\bullet}, \underline{\bullet}$	Upper and lower bounds $\bullet$.
$\langle a, b \rangle$	Inner multiplication between two vectors a and b.

D. Matrices and Vectors

AP_k	Anchor point of the kth objective function.
AP_k^n	The kth normalized anchor point.
$\mathcal{F}^n$	A point in m-dimensional normalized objective space.
$\mathcal{L}_{km}^n$	Normalized increment of Λ_{km}^n.
$U^{WT/PV/D/\ell}$	Vector of certain values for $p_{i,t}^{WT}/p_{i,t}^{PV}/p_{i,t}^D/\ell_{12,t}^{DTR}$.
$\tilde{U}^{WT/PV/D/\ell}$	Vector of uncertain values for $\tilde{p}_{i,t}^{WT}/\tilde{p}_{i,t}^{PV}/\tilde{p}_{i,t}^D/\tilde{\ell}_{12,t}^{DTR}$.
UP_l	The lth utopia hyper-plane point.
X	Vector of decision variables of the D-DNRO model.
Λ_{km}^n	Normalized utopia hyper-plane vectors related to the AP_k.
Π	Payoff matrix.
ϑ	Vector of decision variables of the MOMP problem.

E. Parameters

AF	Adjusting factor.
B	Stefan-Boltzmann constant $[W/(m^2 K^4)]$.
b_i	Shunt susceptance of the line connected to bus $[p.u.]$.
c_i^{MT}	Marginal cost of the MT/PMT units connected to bus $[\$/MWh]$.
c_t^{UP}	Price of buying/selling electrical energy from/to the upstream network at hour $[\$/MWh]$.
c_i^{SU}/c_i^{SD}	Start-up/shutdown cost of the MT/PMT units connected to bus $[\$]$.
c_i^{PMT}	Renting cost of the PMT units connected to bus $[\$]$.
D_{ij}	Outside diameter of the line conductor between buses i and $[m]$.
E_i^{ST-ini}	Initial stored energy of unit i at the beginning of the entire scheduling horizon $[p.u.]$.
g_i	Shunt conductance of the line connected to bus $[p.u.]$.
IC_k	The importance coefficient for $\mathcal{F}_k(\vartheta)$.
k^a	Thermal conductivity of air $[W/m°C]$.
k_{ij}^c	Conductor absorption coefficient for line between buses i and j.
k^f	Solar absorptivity $[kg/m^3]$.
L^f	Flame length $[m]$.

$\ell_{ij,t}^{DTR}$	Squared dynamic current (squared dynamic ampacity) of the line connecting buses i and j at hour t where $\ell_{ij,t}^{DTR} = \left(I_{ij,t}^{DTR}\right)^2$ [$p.u.$].
m	Number of objective functions in MOMP.
mC^p	Total heat capacity of conductor [$J/m°C$].
N^B	Number of buses.
N^S	Number of a posteriori out-of-sample scenarios.
N^T	Number of hours [h].
$p_{i,t}^D/q_{i,t}^D$	Active/reactive load demand connected to bus i at hour [$p.u.$].
$R_{ij}(T^{High})$	AC resistance of conductor between buses i and j at T_{high} [Ω/m].
$R_{ij}(T^{Low})$	AC resistance of conductor between buses i and j at T_{low} [Ω/m].
r_{ij}	Resistance of the line between bus i and j [$p.u.$].
$\overline{|s^{UP}|}$	Limit of apparent power exchange with the upstream network [$p.u.$].
T^f	Flame zone temperature [$°K$].
T^{High}	High average temperate of the line conductor to calculate its AC resistance [$°C$].
T^{Low}	Low average temperature of the line conductor to calculate its AC resistance [$°C$].
UB	Uncertainty budget.
UB^{opt}	Optimal uncertainty budget.
UB_u	Member u of Ω^{UB}.
$\overline{|V_i|}$	Maximum allowable voltage magnitude of bus i [$p.u.$].
$\underline{|V_i|}$	Minimum allowable voltage magnitude of bus i [$p.u.$].
$voll$	Value of lost load [$\$/MWh$].
x_{ij}	Reactance of the line between bus i and j [$p.u.$].
Ψ_{km}	Pre-specified set-point indicating the number of division points on Λ_{km}^n.
γ^f	Flame tilt angle [°].
Δt	Duration of time intervals [h].
ε	Conductor emissivity (0.23 to 0.91).
ε^f	Flame zone emissivity.
η_i^{ST}	Conversion efficiency of the ESS unit connected to bus i.
μ^a	Absolute (dynamic) viscosity of air [$kg/m.s$].
ρ^a	Air density [kg/m^3].
ρ^b	Fuel bulk density [kg/m^3].
τ	Dimensionless atmospheric transmissivity.
ω_{lk}	Weighting parameter related to l^{th} utopia hyper-plane point and the kth objective function of the MOMP problem.

F. Variables

CMB	Crisis management budget [$\$$].
DCC^{UC}	Deterministic commitment-related costs [$\$$].
DDC^{ED}	Deterministic dispatch-related costs [$\$$].
DOC	Deterministic total operation cost [$\$$].
DOC_s	Deterministic total operation cost for scenario vector [$\$$].
E_i^{ST}	Stored electrical energy of the ESS unit connected to bus i [$p.u.$].
EOC	Expected value of total operation cost [$\$$].
EOC_u	Expected value of total operation cost related to member u of Ω^{UB} [$\$$].
$I_{ij,t}$	Current of the line between buses i and j at hour t [$p.u.$].
$I_{ij,t}^{DTR}$	Maximum dynamic current capacity (maximum dynamic ampacity) of the line between buses i and j at hour t [$p.u.$].
$K_{ij,t}^{Angle}$	Wind direction factor for the line between buses i and j at hour t.
$\ell_{ij,t}$	Auxiliary variable indicating the squared current value for the line between buses i and j at hour t [$p.u.$].
$\tilde{\ell}_{12,t}^{DTR}$	Uncertain $\ell_{12,t}^{DTR}$ [$p.u.$].
$N_{ij,t}^{Re}$	Dimensionless Reynolds number for the line between buses i and j at hour t.
$p_{i,t}^{Inject}/q_{i,t}^{Inject}$	Net active/reactive power injection at bus i at hour t [$p.u.$].
$p_{ij,t}^L/q_{ij,t}^L$	Active/reactive power flow of the line connecting buses i and j at hour t [$p.u.$].
$p_{i,t}^{MT/WT/PV}$	Active power generation of (MT, PMT)/WT/PV units connected to bus i at hour t [$p.u.$].
$p_{i,t}^{Shed}/q_{i,t}^{Shed}$	Active/reactive power shedding at bus i at hour t [$p.u.$].

$p_{i,t}^{STC/STD}$	Charging/discharging active power of the ESS unit connected to bus i at hour t $[p.u.]$.
p_t^{UP}/q_t^{UP}	Active/reactive power exchange with the upstream network at hour t $[p.u.]$.
p_t^{UPB}/p_t^{UPs}	Active power to buy/sell from/to the upstream network at hour t $[p.u.]$.
$\tilde{p}_{i,t}^{D}$	Uncertain $p_{i,t}^{D}$ $[p.u.]$.
$\tilde{p}_{i,t}^{PV/WT}$	Uncertain $p_{i,t}^{PV/WT}$ $[p.u.]$.
$q_{ij,t}^{c}$	Convection heat loss rate of the line between buses i and j at hour t $[W/m]$.
$q_{ij,t}^{f}$	Heat gain rate from fire of the line between buses i and j at hour t $[W/m]$.
$q_{i,t}^{MT}$	Reactive power generation of the MT/PMT units connected to bus i at hour t $[p.u.]$.
$q_{ij,t}^{r}$	Radiated heat loss rate of the line between buses i and j at hour t $[W/m]$.
$q_{ij,t}^{s}$	Heat gain rate from sun of the line between buses i and j at hour t $[W/m]$.
$q_{i,t}^{ST}$	Reactive power of the ESS unit connected to bus i at hour t $[p.u.]$.
$R_{ij,t}$	AC resistance of the line conductor between buses i and j at hour t $[\Omega/m]$.
RCC^{UC}	Robust total commitment-related costs $[\$]$.
RDC^{ED}	Robust total dispatch-related costs $[\$]$.
RI	Resiliency index.
RI^{max}	Maximum RI.
RI_u	Resiliency index related to member u of Ω^{UB}.
ROC	Robust total operational cost $[\$]$.
$r_{ij,t}^{f}$	Distance of fire from the line connecting buses i and j at hour t $[m]$.
ru_i^{PMT}	Continuous variable calculating the renting cost of the PMT units connected to bus i $[\$]$.
$su_{i,t}^{MT} / sd_{i,t}^{MT}$	Continuous variables calculating the start-up/shutdown cost of the MT/PMT units connected to bus i at hour t $[\$]$.
sv_k	The kth slack variable.
$T_{ij,t}$	Temperature of the line conductor between buses i and j at hour t $[°C]$.
T_t^a	Ambient air temperature at hour t $[°C]$.
TL_u	Total load during the wildfire for member u of Ω^{UB} $[p.u]$.
TLS_u	Total load shedding during the wildfire for member u of Ω^{UB} $[p.u]$.
$u_{i,t}^{MT}$	Binary variable indicating the status of the MG unit connected to bus i at hour t.
$u_{i,t}^{ST}$	Binary variable indicating the charging/discharging status of the ESS unit connected bus i at hour t.
u_t^{UP}	Binary variable indicating the status of the distribution network in buying/selling electrical energy from/to the upstream system at hour t.
V_t^f	Speed of fire spread at hour t $[m/s]$.
$v_{i,t}$	Auxiliary variable indicating the squared value for voltage magnitude of bus i at hour t $[p.u.]$.
w_t	Wind speed at hour t $[m/s]$.
$\alpha^{WT/PV/D/\ell}$	Envelope bound for the robust region of the uncertain parameter $p_{i,t}^{WT}/p_{i,t}^{PV}/p_{i,t}^{D}/\ell_{12,t}^{DTR}$ $[p.u.]$.
$\delta_{ij,t}^{f}$	Angle of view between the flame and the line conductor between buses i and j $[rad]$.
ϑ_k^{bst}	The value of the decision variables optimizing the kth objective function of the MOMP problem as a single objective optimization.
$\varphi_{ij,t}^{f}$	Radiative heat flux emitted from the fire on the line conductor between buses i and j at hour t $[W/m^2]$.
$\varphi_{ij,t}^{s}$	Solar radiation on the line conductor between buses i and j at hour t $[W/m^2]$.
$\varphi_{ij,t}^{w}$	Angle between the wind direction and the axis of the line conductor between buses i and j at hour t $[rad]$.

1   Introduction

1.1   <u>Motivation and Background</u>

In practice, electrical distribution networks are subject to different catastrophic events (e.g., earthquakes, floods, ice storms, windstorms, wildfires, terroristic attacks, and military actions) [1]. Specifically, the resilience of power systems refers to the capability of the electrical networks to survive low-probability high-impact extreme events efficiently with minimum unserved electricity demand while providing fast restoration to the normal operation state [2, 3]. In recent years, numerous studies have focused on evaluating and enhancing the resilience of electrical distribution networks. These research works can be categorized into (1) long-term hardening-related models with

Table 1: Power systems resiliency studies against wildfire.

Study Type	Resilience Enhancement Technique	Network	DTR Modeling	Wildfire Type	Optimization Type	Uncertain Parameters Considered	Uncertainty Handling Technique	Ref.
Hardening Oriented	Providing the maintenance team with the information of damaged components to quickly identify/restore damaged components	[1]T	T-Lines	Forest wildfire	[3]DO	-	-	[7]
Operation Oriented	Line switching and network reconfiguration	[2]D	-	Urban wildfire	DO	-	-	[8, 9]
	Microgrids, DR, DERs, and optimal load shedding	D	D-Lines	Natural wildfire	[4]NO	Fire Hazard	Probabilistic	[10, 11]
	Optimal load shedding	T	T-Lines	Natural wildfire	DO	-	-	[12]
	Optimal reserve allocation and power production of generation units	D	T-Lines	Natural wildfire	NO	Wind speed/direction	Probabilistic	[13]
	DERs, ESSs, and optimal load shedding	D	Tie-Line	Forest wildfire	NO	Wind/solar power generation	Probabilistic	[14]

Note: [1]T: Transmission, [2]D: Distribution, [3]DO: Deterministic Optimization, [4]NO: Non-Deterministic Optimization.

preventive actions (e.g., utilizing underground distribution lines, upgrading/reinforcing distribution poles/lines with robust materials, and changing the route of distribution lines to secure regions); (2) short-term operation-related models with preventive/corrective actions (e.g., utilizing decentralized control strategies, operating the distribution systems as microgrids, and employing wide-area protection) [4, 5]. Although wildfire is a natural catastrophic event frequently occurring in different areas across the world (e.g., recent disastrous wildfires in Australia, Canada, and United States [6]) and seriously threatening the normal operation of power systems, limited investigations have focused on evaluating and enhancing the resilience of the electrical networks against wildfires through hardening-related [7] or operation-related [8-14] approaches as summarized in Table 1.

In [7], the impact of forest wildfire on the failure probability of transmission lines, and consequently, on the resilience and reliability of the electrical network, has been evaluated by using the dynamic thermal balance equation of transmission lines. Case studies in [7] demonstrate that forest wildfire can significantly affect the resilience and reliability of the electrical network as a function of wildfire, wind speed, and load demand characteristics. In [8], the effect of urban wildfires on the resilience of a distribution network has been evaluated by the Model of Urban Fire Spread (MUFS) software package simulating urban wildfires under different assumptions and conditions. Also, the Dijkstra's algorithm has been used to increase the resilience of the distribution network by finding the optimal switching sequence of normally-open switches for rerouting power along a minimum impedance path. In [9], the proposed model in [8] has been extended to improve the resilience of coupled water and power networks in urban areas during a wildfire. In [10, 11], the resilience of the distribution network under a wildfire has been assessed and enhanced by utilizing microgrids, demand response (DR), and distributed energy resources (DERs), all minimizing the amount of load shedding during a wildfire. Both models in [10, 11] are formulated as a two-stage stochastic optimization problem. The first-stage decisions find the optimal values of commitment variables, which are not a function of the uncertain parameter (i.e., the fire hazard), while the second-stage decisions find the optimal dispatch variables, which are a function of the uncertain parameter. In addition, to enhance the tractability of the problem, the non-linear optimization problem in [10] is recast as a quadratic optimization problem in [11]. In [12], the resilience of a transmission network with dynamic thermal rating (DTR) systems has been evaluated. Also, the resilience has been increased in [12] by minimizing the total operational costs and unserved demands during a natural fire spread.

Since the uncertain nature of wind speed/direction can significantly affect the characteristics of a wildfire spread, a non-deterministic model based on a probabilistic optimal power flow (OPF) has been presented in [13] to enhance the resilience of a DTR-equipped power system during a wildfire through optimal reserve allocation and power production of generation units. In [14], a stochastic optimization model incorporating a multi-period OPF has been utilized to analyze and increase the resilience of distribution networks with DTR systems during a natural fire spread wherein the uncertainties of solar/wind power generations have been characterized by different scenarios. Although the previous research works have addressed several issues related to the resilience of power systems during a wildfire spread across an electrical network, these models have proposed either deterministic approaches neglecting the relevant uncertainties or probabilistic approaches modeling uncertain parameters

through probability distributions. In recent years, different types of uncertain parameters have been mainly quantified by either probability distributions or bounded intervals [15, 16]. Since it may be hard to obtain the exact probability distributions of uncertain parameters in practical applications, particularly in electrical networks with limited historical data, information-gap decision theory (IGDT) as a robust distribution-free method has been used in the power system literature to develop uncertainty-aware models for different investment [17] and operation planning problems [18, 19]. In [17], the IGDT method has been utilized to find a robust plan for investment in transmission lines under the uncertainty of capital costs and electricity demands. In [18], a bidirectional decision-making framework has been introduced based on the notion of the IGDT method to obtain risk-averse and risk-seeker offering strategies for virtual power plants. In [19], a bi-level IGDT-based model has been proposed to obtain robust operational schedules immunized against uncertainties of wind power and DR. In recent years, several resilience-oriented investment/integration planning models based on the notion of IGDT have been presented in the literature. In [20], the IGDT method has been utilized to determine the resilient integration plan for distributed series reactors under extreme events. In [21], a tri-level IGDT-based model has been introduced for investment planning in integrated electric power and natural gas networks to ensure the resilience of coupled energy systems under any disastrous event. In [22], the proposed model in [21] has been extended to find the resilient investment plan in integrated electric power and natural gas networks under both low-frequency high-impact and high-frequency low-impact uncertainties. However, to the best of the authors' knowledge, there is no uncertainty-aware IGDT-based model for the resilient operation of a distribution network under a wildfire spread. Additionally, the AC power flow equations in the previous models have been approximated by inexact linear/quadratic models [11, 14], which may result in inaccuracy or infeasibility of the optimal solution in practical applications. Accordingly, it is essential to develop a proficient non-deterministic approach with low computational complexity and high modeling accuracy for the resilient operation of renewable-integrated distribution networks during the wildfire spread. Against the previous works, this paper presents a resilience-oriented model for the optimal operation of a DTR-equipped distribution network during a wildfire wherein the uncertain load demands and renewable power productions are characterized by the IGDT method and the non-linear/non-convex power flow equations are convexified by a second-order conic transformation.

1.2 Contributions

The main contributions of this paper can be summarized as follows:

- Proposing a multi-horizon IGDT-based model for the resilient operation of a distribution network against unexpected forest wildfires under multifold uncertainties (i.e., wind productions, solar productions, load demands, and ampacity of the DTR-equipped line connecting the distribution network to the bulk electric network). In addition, the proposed model optimizes the renting schedule of portable micro turbines (PMTs), along with other resources, to enhance the resilience of the distribution network against wildfires. To the best of the authors' knowledge, this is a unique feature of the proposed resilient model, which has not been presented in the previous works.
- Utilizing an augmented version of the normalized normal constraint (ANNC) method as a proficient multi-objective optimization approach to solve the proposed multi-horizon IGDT-based model and to obtain a set of evenly distributed Pareto optimal solutions for a specific uncertainty budget (UB). The conservatism level of the optimal solution can be controlled by using UB.
- Finding the best solution among a set of Pareto optimal solutions for a particular value of UB by taking a posteriori out-of-sample analysis simulating the operational performance of the distribution network under different realizations of uncertain parameters. The proposed analysis includes various wildfire-severity scenarios to evaluate the out-of-sample performance of Pareto optimal solutions effectively.
- Introducing a new resilience index to find the optimum crisis management budget (CMB) (i.e., the optimum budget of uncertainty), offering the maximum resilience level. The proposed resilience index concurrently evaluates the operation cost increment, imposed by a wildfire, and load shedding ratio.

1.3 Paper Organization

The rest of this paper is organized as follows. The description of the problem and main modeling assumptions are provided in Section 2. In Section 3, the deterministic formulation of the proposed model is presented for resilient operation planning in DTR-equipped distribution networks during a wildfire spread. In Section 4, first, the non-deterministic formulation of the proposed multi-horizon IGDT-based model is introduced as a multi-objective optimization problem to characterize different uncertainty sources. Subsequently, the ANNC method is utilized to solve the proposed multi-objective model and to find a set of Pareto optimal solutions for a particular UB value.

Afterward, a posteriori out-of-sample analysis is briefly presented to find the best solution among the set of Pareto optimal solutions. In Section 5, the network resilience assessment is outlined to find the optimum CMB offering the maximum resilience level. In Section 6, the proposed deterministic and non-deterministic models are tested on a 33-bus distribution network under different operation conditions to evaluate the performance of the proposed models in enhancing the resilience of the network under a wildfire spread. Finally, Section 7 concludes the paper.

2   Problem Description and Assumptions

This paper presents a multi-horizon IGDT-based model as a multi-objective optimization problem for the distribution network resilient operation (DNRO) encountering unexpected forest wildfires. In general, a forest wildfire may affect a distribution network through (1) damaging the network's components (caused by a wildfire in direct contact with the network) and (2) increasing conductors' temperature (caused by a wildfire nearby and not in direct contact with the network) [10]. The wildfire heat can be transferred via convection and radiation [14]. Since heat transfer through convection may increase conductors' temperature when the wildfire is directly under overhead lines, this type of heat transfer is ignored in this paper, similar to [14]. In summary, the main modeling assumptions of this paper are:

- A radial distribution network is considered.
- It is assumed that the distribution network is connected to the upstream network (i.e., the bulk electric network) at the first hour of the scheduling horizon. However, the distribution network may be disconnected from the upstream network at a later hour due to the spread of the wildfire.
- Only the influence of the wildfire spread on a DTR-equipped line connecting the distribution network to the upstream network is considered in this paper, similar to [10, 14].
- It is assumed that damaged components of the distribution network cannot be repaired, replaced, or restored during the wildfire spread. However, PMTs can be rented for increasing the network resiliency [23].
- The wildfire-associated uncertainties are neglected in this paper, such as uncertainties of wind speed and wind direction, similar to [10, 14]. Moreover, in line with previous research works in the literature, such as [15, 19], characteristic curves of wind turbine (WT) units are used to translate uncertainties of wind speed/direction into uncertainties of power generations of WT units.
- It is assumed that all renewable units are operated at a unity power factor [24].
- The distribution system operator (DSO) is a non-profit organization, and all revenues from selling electricity to consumers belong to retailers [14].

3   Deterministic DNRO Model

In this section, the mathematical formulation of the deterministic DNRO (D-DNRO) model is introduced for the resilient operation of a DTR-equipped distribution network under the wildfire spread. Also, the mathematical formulations for the wildfire spread and the dynamic thermal rating for the line connecting the distribution network to the upstream network are presented in the Appendix (i.e., Section 8). The D-DNRO model, including the objective function (1.a), the economic constraints (1.b)-(1.f), and the technical constraints (1.g)-(1.cc), can be written as follows:

$$\min DOC = \min(DCC^{UC} + DDC^{ED}) \tag{1.a}$$

The objective function of the D-DNRO problem in (1.a) includes total commitment-related and total dispatch-related costs, denoted by DCC^{UC} and DDC^{ED}, respectively.

subject to:

Commitment-Related Costs:

$$DCC^{UC} = \sum_{t=1}^{N^T} \sum_{i=1}^{N^B} \left(su_{i,t}^{MT} + sd_{i,t}^{MT} + ru_i^{PMT} \right) \tag{1.b}$$

The commitment-related costs DCC^{UC} in (1.b) consists of total start-up and shut-down costs for the MT/PMT units as well as the renting costs of PMT units.

Dispatch-Related Costs:

$$DDC^{ED} = \sum_{t=1}^{N^T} \sum_{i=1}^{N^B} voll \cdot p_{i,t}^{Shed} + \sum_{t=1}^{N^T} \sum_{i=1}^{N^B} c_i^{MT} \cdot p_{i,t}^{MT} + \sum_{t=1}^{N^T} c_t^{UP} \cdot \left(p_t^{UP_B} - p_t^{UP_S} \right) \tag{1.c}$$

The dispatch-related costs in (1.c) consist of total costs of load shedding, total generation costs for the MT/PMT units, and total costs/revenues of buying/selling electrical energy from/to the upstream network. Also, without loss of generality, the generation cost of each MT/PMT unit is modeled by a linear function [14].

Constraints on Commitment-Related Variables of MT/PMT Units:

$$su_{i,t}^{MT} \geq 0, su_{i,t}^{MT} \geq c_i^{SU} \cdot \left(u_{i,t}^{MT} - u_{i,t-1}^{MT}\right) \quad \forall i, \forall t \tag{1.d}$$

$$sd_{i,t}^{MT} \geq 0, sd_{i,t}^{MT} \geq c_i^{SD} \cdot \left(u_{i,t-1}^{MT} - u_{i,t}^{MT}\right) \quad \forall i, \forall t \tag{1.e}$$

$$ru_i^{PMT} \geq 0, ru_i^{PMT} \geq c_i^{PMT} \cdot \left(u_{i,t}^{MT} - u_{i,t-1}^{MT}\right) \quad \forall i, \forall t \tag{1.f}$$

Constraints (1.d)-(1.f) calculate the start-up, shut-down, and renting costs, respectively.

Constraints on Net Power Injection:

$$p_{t|i=1}^{UP} + p_{i,t}^{MT} + p_{i,t}^{WT} + p_{i,t}^{PV} + p_{i,t}^{STD} - p_{i,t}^{STC} - p_{i,t}^{D} + p_{i,t}^{Shed} = p_{i,t}^{Inject} \quad \forall i, \forall t \tag{1.g}$$

$$q_{t|i=1}^{UP} + q_{i,t}^{MT} + q_{i,t}^{ST} - q_{i,t}^{D} + q_{i,t}^{Shed} = q_{i,t}^{Inject} \quad \forall i, \forall t \tag{1.h}$$

Constraints (1.g) and (1.h) represent the net active and reactive power injection at each bus during the scheduling horizon. It is assumed that $i = 1$ indicates the connection point to the upstream network.

Constraints on Power Generations of MT, PMT, WT, and PV Units:

$$\underline{p_i^{MT}} \cdot u_{i,t}^{MT} \leq p_{i,t}^{MT} \leq \overline{p_i^{MT}} \cdot u_{i,t}^{MT} \quad \forall i, \forall t \tag{1.i}$$

$$\underline{q_i^{MT}} \cdot u_{i,t}^{MT} \leq q_{i,t}^{MT} \leq \overline{q_i^{MT}} \cdot u_{i,t}^{MT} \quad \forall i, \forall t \tag{1.j}$$

$$0 \leq p_{i,t}^{WT} \leq \overline{p_i^{WT}} \quad \forall i, \forall t \tag{1.k}$$

$$0 \leq p_{i,t}^{PV} \leq \overline{p_i^{PV}} \quad \forall i, \forall t \tag{1.l}$$

Constraints (1.i) and (1.j) limit the active and reactive power of the MT/PMT units, respectively, while constraints (1.k) and (1.l) limit the active power of the WT and photovoltaic (PV) units, respectively.

Constraints on Line Flows:

$$p_{i,t}^{Inject} = \sum_{\substack{h=1 \\ h \neq i}}^{N^B} p_{ih,t}^{L} - \sum_{\substack{j=1 \\ j \neq i}}^{N^B} \left(p_{ji,t}^{L} - r_{ij} \cdot \ell_{ji,t}\right) + g_i \cdot v_{i,t} \quad \forall i, \forall t \tag{1.m}$$

$$q_{i,t}^{Inject} = \sum_{\substack{h=1 \\ h \neq i}}^{N^B} q_{ih,t}^{L} - \sum_{\substack{j=1 \\ j \neq i}}^{N^B} \left(q_{ji,t}^{L} - x_{ij} \cdot \ell_{ji,t}\right) + b_i \cdot v_{i,t} \quad \forall i, \forall t \tag{1.n}$$

$$v_{i,t} = v_{j,t} - 2 \cdot \left(r_{ij} \cdot p_{ji,t}^{L} + x_{ij} \cdot q_{ji,t}^{L}\right) + \left(r_{ij}^2 + x_{ij}^2\right) \cdot \ell_{ji,t} \quad \forall (i,j), \forall t \tag{1.o}$$

$$\underline{|V_i|}^2 \leq v_{i,t} \leq \overline{|V_i|}^2 \quad \forall i, \forall t \tag{1.p}$$

$$\ell_{ij,t} \geq \frac{\left(p_{ij,t}^{L}\right)^2 + \left(q_{ij,t}^{L}\right)^2}{v_{i,t}} \quad \forall (i,j), \forall t \tag{1.q}$$

Constraints (1.m) and (1.n) denote the active and reactive power balance at each hour of the scheduling horizon. Also, constraint (1.o) finds the voltage drop between the connected buses of the distribution network, while constraint (1.p) bounds the voltage magnitudes at each bus. Constraint (1.q) represents the relationship between the current and voltage as well as the active and reactive powers for each line by a second-order conic relaxation [25].

Constraint on DTR of the Overhead Tie-Line:

$$\ell_{t|ij=12} \leq \ell_{t|ij=12}^{DTR} \quad \forall t \tag{1.r}$$

Constraint (1.r) denotes the DTR limit for the overhead tie-line, between bus $i = 1$ and bus $j = 2$, connecting the distribution network to the upstream grid.

Constraints on Load Shedding:

$$0 \leq p_{i,t}^{Shed} \leq p_{i,t}^{D} \quad \forall i, \forall t \tag{1.s}$$

$$q_{i,t}^{Shed} = p_{i,t}^{Shed} \cdot \frac{q_{i,t}^{D}}{p_{i,t}^{D}} \quad \forall i, \forall t \tag{1.t}$$

Constraint (1.s) bounds the value of load shedding at each bus and constraint (1.t) enforces a linear relation between active and reactive load shedding.

Constraints on Charging/Discharging of ESS Units:

$$\sum_{t=1}^{N^T}\left(\eta_i^{ST}\cdot p_{i,t}^{STC}-\frac{p_{i,t}^{STD}}{\eta_i^{ST}}\right)=0 \quad \forall i \tag{1.u}$$

$$\underline{E_i^{ST}}\le E_i^{ST-ini}+\overbrace{\sum_{\tau=1}^{t}\left(\eta_i^{ST}\cdot p_{i,\tau}^{STC}-\frac{p_{i,\tau}^{STD}}{\eta_i^{ST}}\right)}^{E_{i,t}^{ST}}\le \overline{E_i^{ST}} \quad \forall i,\forall t \tag{1.v}$$

$$0\le p_{i,t}^{STC}\le \overline{p_i^{STC}}\cdot u_{i,t}^{ST} \quad \forall i,\forall t \tag{1.w}$$

$$0\le p_{i,t}^{STD}\le \overline{p_i^{STD}}\cdot\left(1-u_{i,t}^{ST}\right) \quad \forall i,\forall t \tag{1.x}$$

$$\underline{q_i^{ST}}\le q_{i,t}^{ST}\le \overline{q_i^{ST}} \quad \forall i,\forall t \tag{1.y}$$

Constraint (1.u) ensures that the stored energies of each energy storage system (ESS) at the initial and final hours of the scheduling horizon are equal. Also, constraint (1.v) limits the maximum and minimum stored energy of each ESS unit during all scheduling hours. Constraints (1.w) and (1.x) impose the charging and discharging limits of each ESS unit, respectively [26]. Furthermore, constraint (1.y) represents the reactive power limitations of ESS units [14, 27].

Constraints on Power Exchange with the Upstream Network:

$$p_t^{UP}=p_t^{UPB}-p_t^{UPS} \quad \forall t \tag{1.z}$$

$$0\le p_t^{UPB}\le \overline{|s^{UP}|}\cdot u_t^{UP} \quad \forall t \tag{1.aa}$$

$$0\le p_t^{UPS}\le \overline{|s^{UP}|}\cdot(1-u_t^{UP}) \quad \forall t \tag{1.bb}$$

$$(p_t^{UP})^2+(q_t^{UP})^2\le \overline{|s^{UP}|}^2 \quad \forall t \tag{1.cc}$$

Constraint (1.z) calculates the active power exchange with the upstream network. Constraints (1.aa) and (1.bb) limit the capacity of buying/selling active power from/to the upstream network, respectively [14]. Also, (1.cc) bounds the apparent power exchange with the upstream network. The D-DNRO model in (1.a)-(1.cc) as a mixed-integer second-order conic programming (MISOCP) problem can be rewritten in a compact form as given below:

$$\min_{X\in\Xi^D}\overbrace{OF\big(X,\widetilde{U}^{WT},\widetilde{U}^{PV},\widetilde{U}^{D},\widetilde{U}^{\ell}\big)}^{DOC} \tag{2}$$

where X refers to the vector of decision variables of the D-DNRO model, and $\Xi^D\big(\widetilde{U}^{WT},\widetilde{U}^{PV},\widetilde{U}^{D},\widetilde{U}^{\ell}\big)$ denotes the solution space of the D-DNRO problem constructed by constraints (1.b)-(1.cc). Note that vectors of uncertain parameters (i.e., $\widetilde{U}^{WT}$, $\widetilde{U}^{PV}$, $\widetilde{U}^{D}$, and $\widetilde{U}^{\ell}$) in D-DNRO as the deterministic model are fixed to their forecast values (i.e., $\widetilde{U}^{WT}=U^{WT}$, $\widetilde{U}^{PV}=U^{PV}$, $\widetilde{U}^{D}=U^{D}$, and $\widetilde{U}^{\ell}=U^{\ell}$).

4   Robust DNRO Model

In this section, the IGDT-DNRO model is introduced as a multi-objective optimization problem to characterize the uncertainties pertaining to power generations of WT and PV units, load demands, and DTR of the tie-line connecting the distribution network to the upstream network. Then, the ANNC approach is utilized for solving the proposed multi-objective IGDT-DNRO formulation.

4.1   The Proposed IGDT-Based Resilient Operation Formulation

IGDT, as a distribution-free uncertainty-aware optimization model, finds optimal solutions immunized against any realization of uncertain parameters lying within bounded sets designated as robust regions. In general, the IGDT method can be utilized as a risk-averse or a risk-seeker framework. The risk-averse/seeker IGDT model employs a pessimistic/optimistic criterion to maximize/minimize unfavorable/favorable deviations of uncertain parameters from their forecast values [18]. Moreover, a single-horizon IGDT model only characterizes one uncertain parameter through a robust region while a multi-horizon IGDT model concurrently characterizes multiple uncertain parameters through multiple robust regions. In summary, the aim of a risk-averse strategy is to maximize robust regions of uncertain parameters where the objective function of the non-deterministic problem is bounded using a specific parameter named budget of uncertainty [28]. The main advantages of the IGDT method

compared to other uncertainty characterization models are (i) needing limited historical data to obtain a robust solution and (ii) enforcing a low computational complexity due to needing a limited number of auxiliary variables/constraints to characterize uncertainties [17, 18].

In this paper, a risk-averse multi-horizon IGDT strategy is proposed to evaluate the resilience of a distribution network considering wildfires under worst-case realizations of uncertain parameters. Furthermore, a set of different values for the budget of uncertainty is considered to evaluate the effect of varying the robustness level of the IGDT model on the distribution network resilience level as given below:

$$\Omega^{UB} = \{UB_u \mid UB_u = 0.40 \cdot u\} \quad \forall u = 0,1,2,3, \dots \tag{3}$$

Also, the envelope-bound model is utilized to define robust regions characterizing the uncertainties of power generations of WT units ($\tilde{p}_{i,t}^{WT}$), power generations of PV units ($\tilde{p}_{i,t}^{PV}$), load demands ($\tilde{p}_{i,t}^{D}$), and DTR of the tie-line connecting the distribution network to the upstream network ($\tilde{\ell}_{12,t}^{DTR}$) as given below [17]:

$$\Gamma^{WT}\big(\tilde{p}_{i,t}^{WT}, \alpha^{WT}\big) = \left\{\tilde{p}_{i,t}^{WT} : \left|\frac{\tilde{p}_{i,t}^{WT} - p_{i,t}^{WT}}{p_{i,t}^{WT}}\right| \leq \alpha^{WT}, \alpha^{WT} \geq 0\right\} \quad \forall i, \forall t \tag{4.a}$$

$$\Gamma^{PV}\big(\tilde{p}_{i,t}^{PV}, \alpha^{PV}\big) = \left\{\tilde{p}_{i,t}^{PV} : \left|\frac{\tilde{p}_{i,t}^{PV} - p_{i,t}^{PV}}{p_{i,t}^{PV}}\right| \leq \alpha^{PV}, \alpha^{PV} \geq 0\right\} \quad \forall i, \forall t \tag{4.b}$$

$$\Gamma^{D}\big(\tilde{p}_{i,t}^{D}, \alpha^{D}\big) = \left\{\tilde{p}_{i,t}^{D} : \left|\frac{\tilde{p}_{i,t}^{D} - p_{i,t}^{D}}{p_{i,t}^{D}}\right| \leq \alpha^{D}, \alpha^{D} \geq 0\right\} \quad \forall i, \forall t \tag{4.c}$$

$$\Gamma^{\ell}\big(\tilde{\ell}_{12,t}^{DTR}, \alpha^{\ell}\big) = \left\{\tilde{\ell}_{12,t}^{DTR} : \left|\frac{\tilde{\ell}_{12,t}^{DTR} - \ell_{12,t}^{DTR}}{\ell_{12,t}^{DTR}}\right| \leq \alpha^{\ell}, \alpha^{\ell} \geq 0\right\} \quad \forall i, \forall t \tag{4.d}$$

where the auxiliary variables α^{WT}, α^{PV}, α^{D}, and α^{ℓ} bound the variation intervals of the uncertainties $\tilde{p}_{i,t}^{WT}$, $\tilde{p}_{i,t}^{PV}$, $\tilde{p}_{i,t}^{D}$ and $\tilde{\ell}_{12,t}^{DTR}$ belonging to the robust regions Γ^{WT}, Γ^{PV}, Γ^{D}, and Γ^{ℓ}, respectively. According to the IGDT concept [29], the robust regions of uncertainties can be obtained by solving a risk-averse multi-objective optimization problem as follows:

$$\max\big(\alpha^{WT}, \alpha^{PV}, \alpha^{D}, \alpha^{\ell}\big) \tag{5.a}$$

subject to:

$$ROC \equiv \max_{X, \tilde{U}^{WT}, \tilde{U}^{PV}, \tilde{U}^{D}, \tilde{U}^{\ell}} OF\big(X, \tilde{U}^{WT}, \tilde{U}^{PV}, \tilde{U}^{D}, \tilde{U}^{\ell}\big) \leq DOC \cdot (1 + UB_u) \tag{5.b}$$

$$X \in \Xi^{\text{IGDT}}\big(\tilde{U}^{WT}, \tilde{U}^{PV}, \tilde{U}^{D}, \tilde{U}^{\ell}\big) \; ; \; \tilde{U}^{WT} \in \Gamma^{WT} \; ; \; \tilde{U}^{PV} \in \Gamma^{PV} \; ; \; \tilde{U}^{D} \in \Gamma^{D} \; ; \; \tilde{U}^{\ell} \in \Gamma^{\ell} \; ; \; UB_u \in \Omega^{UB} \tag{5.c}$$

The objective function of the IGDT-DNRO problem in (5.a) maximizes the envelope bounds α^{WT}, α^{PV}, α^{D} and α^{ℓ} of the uncertain parameters $\tilde{p}_{i,t}^{WT}$, $\tilde{p}_{i,t}^{PV}$, $\tilde{p}_{i,t}^{D}$ and $\tilde{\ell}_{12,t}^{DTR}$ to maximize the solution robustness. Also, constraint (5.b) bounds the robust total operation cost (i.e., ROC) by means of the deterministic total operation cost (i.e., DOC), obtained from solving the D-DNRO problem in (1.a)-(1.cc), and the uncertainty budget (i.e., UB_u). Moreover, constraint (5.c) presents the feasible space of the IGDT-DNRO problem. Since the robust total operation costs can be obtained by adopting worst-case realizations for all uncertain parameters, constraints (5.b) and (5.c) in the IGDT-DNRO model can be rewritten as follows:

$$ROC \equiv \max_{X} OF\big(X, U^{WT} \cdot (1 - \alpha^{WT}), U^{PV} \cdot (1 - \alpha^{PV}), U^{D} \cdot (1 + \alpha^{D}), U^{\ell} \cdot (1 - \alpha^{\ell})\big) \leq DOC \cdot (1 + UB_u) \tag{6}$$

$$X \in \Xi^{D}\big(U^{WT} \cdot (1 - \alpha^{WT}), U^{PV} \cdot (1 - \alpha^{PV}), U^{D} \cdot (1 + \alpha^{D}), U^{\ell} \cdot (1 - \alpha^{\ell})\big) \; ; \; UB_u \in \Omega^{UB} \tag{7}$$

Therefore, considering (6) and (7), the extended form of the IGDT-DNRO model as a multi-objective optimization problem, including the objective function (8.a), the economic constraints (8.b)-(8.e) and (1.d)-(1.f), and technical constraints (8.f)-(8.i), (1.i)-(1.q), and (1.t)-(1.cc), can be presented as given below:

$$\max\big(\alpha^{WT}, \alpha^{PV}, \alpha^{D}, \alpha^{\ell}\big) \tag{8.a}$$

subject to:

$$ROC \leq DOC \cdot (1 + UB_u) \tag{8.b}$$

$$ROC = RDC^{UC} + RCC^{ED} \tag{8.c}$$

$$RDC^{UC} = \sum_{t=1}^{N^T} \sum_{i=1}^{N^B} \big(su_{i,t}^{MT} + sd_{i,t}^{MT} + ru_i^{PMT}\big) \tag{8.d}$$

$$RCC^{ED} = \sum_{t=1}^{N^T} \sum_{i=1}^{N^B} voll \cdot p_{i,t}^{Shed} + \sum_{t=1}^{N^T} \sum_{i=1}^{N^B} c_i^{MT} \cdot p_{i,t}^{MT} + \sum_{t=1}^{N^T} c_t^{UP} \cdot \left(p_t^{UP_B} - p_t^{UP_S}\right) \tag{8.e}$$

$$p_{t|i=1}^{UP} + p_{i,t}^{MT} + \left[p_{i,t}^{WT} \cdot (1 - \alpha^{WT})\right] + \left[p_{i,t}^{PV} \cdot (1 - \alpha^{PV})\right] + p_{i,t}^{STD} - p_{i,t}^{STC} - \left[p_{i,t}^{D} \cdot (1 + \alpha^{D})\right] + p_{i,t}^{Shed}$$
$$= p_{i,t}^{Inject} \quad \forall i, \forall t \tag{8.f}$$

$$q_{t|i=1}^{UP} + q_{i,t}^{MT} + q_{i,t}^{ST} - \left[q_{i,t}^{D} \cdot (1 + \alpha^{D})\right] + q_{i,t}^{Shed} = q_{i,t}^{Inject} \quad \forall i, \forall t \tag{8.g}$$

$$\ell_{t|ij=12} \leq \ell_{t|ij=12}^{DTR}\left(1 - \alpha^{\ell}\right) \quad \forall t \tag{8.h}$$

$$0 \leq p_{i,t}^{Shed} \leq \left[p_{i,t}^{D} \cdot (1 + \alpha^{D})\right] \quad \forall i, \forall t \tag{8.i}$$

$$(1.d)-(1.f), (1.i)-(1.q) \text{ and } (1.t)-(1.cc) \tag{8.j}$$

In this paper, the IGDT-DNRO model in (8.a)-(8.j), as a multi-objective MISOCP problem, is solved by the ANNC method to obtain the Pareto optimal solution, as described in the sequel.

4.2 Augmented Normalized Normal Constraint Method

The normalized normal constraint (NNC) method is a systematic multi-objective optimization method offering uniformly distributed Pareto optimal solutions for a multi-objective mathematical programming (MOMP) problem by reducing the feasible objective space [28]. In this paper, ANNC as the augmented version of the original NNC method is utilized. The main advantages of the ANNC method compared to other MOMP ones are (i) providing Pareto optimal solutions by dividing the objective space into feasible and infeasible spaces [30], (ii) finding non-dominated solutions [18], (iii) increasing the accuracy and tractability of the MOMP problem [31]. Without loss of generality, it is assumed that all objective functions of an MOMP problem should be maximized. Thus, an MOMP problem can be written as follows:

$$\max_{\vartheta \in \Xi^{MOMP}} \{\mathcal{F}_1(\vartheta), \cdots, \mathcal{F}_k(\vartheta), \cdots, \mathcal{F}_m(\vartheta)\} \tag{9}$$

where (9) represents the general form of an MOMP problem. In the following, the ANNC method is summarized step by step.

Step 1: Constructing the anchor points) Find the optimal value of the kth objective function as follows:

$$\mathcal{F}_k^{bst}\left(\vartheta_k^{bst}\right) = \max_{\vartheta \in \Xi^{MOMP}} \{\mathcal{F}_k(\vartheta)\} \quad \forall k \in \{1, \cdots, m\} \tag{10}$$

Then, substitute the optimal decision vector ϑ_k^{bst} in the other $m - 1$ objective functions (i.e., $\mathcal{F}_z\left(\vartheta_k^{bst}\right) \ \forall z \in \{1, \cdots, k-1, k+1, \cdots, m\}$) to obtain the anchor point of the kth objective function, denoted as AP_k.

Step 2: Constructing the payoff matrix) Place all anchor points (i.e., $AP_k, \forall k \in \{1, \cdots, m\}$) in a column array to construct the payoff matrix Π, as denoted by (11):

$$\Pi \triangleq \begin{bmatrix} AP_1 \\ \vdots \\ AP_k \\ \vdots \\ AP_m \end{bmatrix} = \begin{bmatrix} \mathcal{F}_1^{bst}(\vartheta_1^{bst}) & \cdots & \mathcal{F}_k(\vartheta_1^{bst}) & \cdots & \mathcal{F}_m(\vartheta_1^{bst}) \\ \vdots & \ddots & \vdots & \vdots & \vdots \\ \mathcal{F}_1(\vartheta_k^{bst}) & \cdots & \mathcal{F}_k^{bst}(\vartheta_k^{bst}) & \cdots & \mathcal{F}_m(\vartheta_k^{bst}) \\ \vdots & \vdots & \vdots & \ddots & \vdots \\ \mathcal{F}_1(\vartheta_m^{bst}) & \cdots & \mathcal{F}_k(\vartheta_m^{bst}) & \cdots & \mathcal{F}_m^{bst}(\vartheta_m^{bst}) \end{bmatrix} \tag{11}$$

Step 3: Normalizing all objective functions of MOMP) All objective functions need to be normalized within the interval [0,1]. For this purpose, find the best, i.e., $\mathcal{F}_k^{bst}\left(\vartheta_k^{bst}\right)$, and the worst, i.e., $\mathcal{F}_k^{wst}\left(\vartheta_k^{bst}\right)$, values of the kth column in the payoff matrix. Then, normalize the objective functions as follows:

$$\mathcal{F}_k^n(\vartheta) = \frac{\mathcal{F}_k(\vartheta) - \mathcal{F}_k^{wst}\left(\vartheta_k^{bst}\right)}{\mathcal{F}_k^{bst}(\vartheta_k^{bst}) - \mathcal{F}_k^{wst}(\vartheta_k^{bst})} \quad \forall k \in \{1, \cdots, m\} \tag{12}$$

Step 4: Generating normalized utopia hyper-plane vectors) Connect all anchor points to construct the utopia hyper-plane. Then, generate the normalized utopia hyper-plane vectors (Λ_{km}^n) as below:

$$\Lambda_{km}^n = AP_m^n - AP_k^n \quad \forall k \in \{1, \cdots, m-1\} \tag{13}$$

Step 5: Obtaining the normalized incremental utopia hyper-plane vectors) The normalized incremental utopia hyper-plane vectors ($\mathcal{L}_{km}^n$) are added to utopia hyper-plane points in the path of each utopia hyper-plane vector to obtain the next utopia hyper-plane point. Determine each normalized increment utopia hyper-plane vector as follows:

$$\mathcal{L}_{km}^n = \frac{\|\Lambda_{km}^n\|}{\Psi_{km} - 1} \qquad \forall k \in \{1, \cdots, m-1\} \tag{14.a}$$

where Ψ_{km} denotes the number of utopia hyper-plane points on Λ_{km}^n. Then, to uniformly distribute the utopia hyper-plane points on Λ_{km}^n, relate all values of Ψ_{km} to each other as given below:

$$\Psi_{km} = \frac{\Psi_{1m}\|\Lambda_{km}^n\|}{\|\Lambda_{1m}^n\|} \qquad \forall k \in \{1, \cdots, m-1\} \tag{14.b}$$

Based on (14.b), the number of utopia hyper-plane points related to Λ_{km}^n depends on its Euclidian norm (i.e., $\|\Lambda_{km}^n\|$) and Ψ_{1m} (a pre-specified set-point).

Step 6: Generating utopia hyper-plane points) Calculate the lth utopia hyper-plane point (UP_l) based on the weighted linear combination of the normalized anchor points as follows:

$$UP_l = \sum_{k=1}^{m} \omega_{lk} \cdot AP_k^n \tag{15.a}$$

where

$$0 \le \omega_{lk} \le 1 \tag{15.b}$$

$$\sum_{k=1}^{m} \omega_{lk} = 1 \tag{15.c}$$

To calculate each UP_l, the weighting parameters (i.e., ω_{lk}) need to be changed within the interval $[0,1]$. In this paper, the MOMP has four objectives (i.e., $m = 4$). Also, it is assumed $\Psi_{km} = 5$. Therefore, the set of ω_{lk} values, according to (15.b) and (15.c), can be obtained as given below:

$$
\begin{aligned}
&(\omega_{l1}, \omega_{l2}, \omega_{l3}, \omega_{l4}) \\
&= \left\{ \begin{array}{l}
(1.00,0.00,0.00,0.00), (0.75,0.25,0.00,0.00), (0.75,0.00,0.25,0.00), (0.75,0.00,0.00,0.25), (0.50,0.50,0.00,0.00), \\
(0.50,0.25,0.25,0.00), (0.50,0.25,0.00,0.25), (0.50,0.00,0.50,0.00), (0.50,0.00,0.25,0.25), (0.50,0.00,0.00,0.50), \\
(0.25,0.75,0.00,0.00), (0.25,0.50,0.25,0.00), (0.25,0.50,0.00,0.25), (0.25,0.25,0.50,0.00), (0.25,0.25,0.25,0.25), \\
(0.25,0.25,0.00,0.50), (0.25,0.00,0.75,0.00), (0.25,0.00,0.50,0.25), (0.25,0.00,0.25,0.50), (0.25,0.00,0.00,1.00), \\
(0.00,1.00,0.00,0.00), (0.00,0.75,0.25,0.00), (0.00,0.75,0.00,0.25), (0.00,0.50,0.50,0.00), (0.00,0.50,0.25,0.25), \\
(0.00,0.50,0.00,0.50), (0.00,0.25,0.75,0.00), (0.00,0.25,0.50,0.25), (0.00,0.25,0.25,0.50), (0.00,0.25,0.00,0.75), \\
(0.00,0.00,1.00,0.00), (0.00,0.00,0.75,0.25), (0.00,0.00,0.50,0.50), (0.00,0.00,0.25,0.75), (0.00,0.00,0.00,1.00)
\end{array} \right\}
\end{aligned}
$$

Step 7: Producing a Pareto solution for each utopia hyper-plane point) Generate a Pareto solution for each UP_l through solving the following optimization problem:

$$\max_{\vartheta \in \Xi^{MOMP}} \mathcal{F}_m(\vartheta) + AF \cdot \sum_{k=1}^{m-1} \left(\frac{IC_k}{IC_m}\right) \cdot sv_k \tag{16.a}$$

$s.t.$

$$\langle \mathcal{F}^n - UP_l, \Lambda_{km}^n \rangle + sv_k = 0 \quad sv_k \ge 0 \quad \forall k \in \{1, \cdots, m-1\} \tag{16.b}$$

Note that the objective function of the ANNC model in (16.a) includes the slack variables (i.e., sv_k) weighted by importance coefficients (i.e., IC_k) where IC_k denotes the importance coefficient of $\mathcal{F}_k$. Thus, IC_k/IC_m represents the relative importance coefficient of $\mathcal{F}_k$ with respect to $\mathcal{F}_m$. In other words, the ANNC method maximizes a single objective function with the slack variables based on the relative importance coefficients. If the values of the slack variables increase, the dot products $\langle \mathcal{F}^n - UP_l, \Lambda_{km}^n \rangle$ with negative values in (16.b) take higher absolute values, meaning the angles between vector $\mathcal{F}^n - UP_l$ and Λ_{km}^n increase. The adjusting factor AF in (16.a) is utilized to enhance the flexibility of the proposed ANNC method. Also, $\mathcal{F}^n$ is a point in the normalized objective space. According to (16.b), the feasible space is reduced to a subspace enclosed by the normal hyper-planes where each normal hyper-plane is perpendicular to a utopia hyper-plane vector. It is noteworthy to mention that the constraints (16.b) are added to the initial constraints of the MOMP problem. Thus, $\Xi^{MOMP} = \Xi^{IGDT}$ including (8.b)-(8.j) in addition to the constraints of the objective space in (16.b).

The MOMP problem of the IGDT-DNRO model presented in (8.a)-(8.j) with four objective functions can be solved by the aforementioned ANNC method. In this work, a posteriori out-of-sample analysis is presented for determining the best solution among the set of Pareto solutions generated by the ANNC method for all allowed values of the budget of uncertainty in Ω^{UB}.

4.3   A Posteriori Out-of-Sample Analysis

In this paper, a posteriori out-of-sample analysis including scenarios with diverse wildfire severities for the ampacity of the tie-line is undertaken to obtain the best solution among the set of Pareto optimal solutions for the resilient operation of the distribution network under wildfire spread. Evaluation of each Pareto optimal solution (which is found by solving the multi-objective IGDT-DNRO model for a specific budget of uncertainty) by a posteriori out-of-sample analysis can be summarized as below [28]:

Step 1) Set $s = 0$ and fix all binary variables to the optimal values obtained from solving the IGDT-DNRO problem for a specific $UB_u \in \Omega^{UB}$. Therefore, IGDT-DNRO as an MISOCP problem boils down into a second-order conic programming (SOCP) problem.

Step 2) Identify the total number of scenarios (i.e., N^S). Then, define N^S wildfire severity scenarios.

Step 3) Solve the SOCP optimization problem of each scenario s to obtain its DOC (i.e., DOC_s).

Step 4) If $s < N^S$, return to Step 3. Otherwise, obtain and report $EOC = \frac{\sum_{s=1}^{N^S} DOC_s}{N^S}$.

It is noteworthy to mention that a posteriori out-of-sample analysis needs to be run for all Pareto optimal solutions to obtain the best solution offering the minimum expected operation cost (EOC) for each specific $UB_u \in \Omega^{UB}$.

5   Resilience Assessment with Optimal Crisis Management Budget

5.1   Proposed Resilience Index

There are several indices for resilience assessment of power systems, which have been thoroughly reviewed and discussed in [2, 32]. In this paper, the resilience assessment of a distribution network is investigated during a wildfire event. It is a common approach in the literature to quantify the resilience of the network based on the amount of loss of load under extreme events [2, 33]. It is noteworthy to mention that different quantities and measures can be considered for evaluating the resilience level of the network, such as loss of load, expected operation cost, and the maximum DTR level for all lines of the network. The maximum DTR level for all lines of the network depends on the importance of each line while the importance of lines can change dynamically due to continuous changes in loading conditions of the network [34]. Furthermore, the maximum DTR level can implicitly affect the loss of load and the expected operation cost. Therefore, a new resiliency index is proposed in this research work, which concurrently considers both loss of load and expected operation cost, encountering a wildfire:

$$TL_u = \sum_{t=1}^{N^T} \sum_{i=1}^{N^B} p_{i,t}^D \cdot (1 + \alpha^D) \quad \forall u \tag{17.a}$$

$$TLS_u = \sum_{t=1}^{N^T} \sum_{i=1}^{N^B} p_{i,t}^{Shed} \quad \forall u \tag{17.b}$$

$$RI_u = \frac{TL_u}{1 + TLS_u} \times \frac{1}{EOC_u} \quad \forall u \tag{17.c}$$

where, (17.a) and (17.b) denote the total load and total load shedding during the wildfire for member u of Ω^{UB}, respectively. Also, (17.c) represents the proposed resiliency index (RI) for member u of Ω^{UB}. As depicted in (17.c), the resilience index is calculated using the ratio of the total load (i.e., TL_u) to the total load shedding (i.e., TLS_u) and the inverse of the expected operation cost (i.e., EOC_u) for member u of Ω^{UB}. The number one in the denominator $1 + TLS_u$ is to avoid the adverse effects of load shedding values close to zero. Based on the proposed resiliency index, a solution with a lower load shedding ratio and lower incremental operation cost, encountering wildfire scenarios, will have higher resiliency. The theoretical range of the proposed resiliency index is $[0, +\infty)$; however, its practical range depends on the technical and operational characteristics of the distribution network. In this paper, the value of the resilience index is used to find the optimal CMB as discussed in the sequel.

5.2   Finding Optimal CMB with Maximum Resilience Level

After the occurrence of catastrophic events, network resources and facilities need to be optimally utilized in order to reduce potential consequences and recover the initial state as rapidly as possible. In this paper, the term CMB refers to a specific budget of uncertainty, as a member of the set of allowed values for the budget of uncertainty

(i.e., $UB_u \in \Omega^{UB}$), which results in the maximum resilience index. The proposed framework for determining the optimal CMB is outlined in Fig. 1. According to Fig. 1, the optimal CMB can be determined by means of a four-layer framework including: (1) data processing, (2) DNRO model, (3) resilience assessment, and (4) optimal CMB determination, where all layers consist of 15 steps, indicated by numbers within circles.

First Layer (Data Processing): In the first layer (steps 1-5), the required data can be prepared by utilizing fire data (flame and fuel characterization) and weather data (wind data), as discussed in Section 8.1. Furthermore, DTR data (i.e., the tie-line ampacity) can be prepared by utilizing weather data (i.e., wind, solar, and temperature data) as well as network data (outside diameter of the line conductors), as discussed in Section 8.2.

Second Layer (DNRO Model): The second layer (steps 6-12) includes the proposed DNRO framework consisting of D-DNRO and IGDT-DNRO models. The input data of these models are network parameters as well as DTR data. The D-DNRO model, including the total load shedding of the distribution network at each hour of the scheduling horizon, is optimized to calculate DOC, as described in Section 3. The optimal solution of the D-DNRO model is then utilized by the proposed framework to solve the IGDT-DNRO model for a specific $UB_u \in \Omega^{UB}$, as discussed in Section 4.1. The IGDT-DNRO model, as a multi-objective optimization problem, is solved using the ANNC method to find a set of Pareto optimal solutions for each member of Ω^{UB}, as explained in Section 4.2. Additionally, a posteriori out-of-sample analysis is used to obtain the best solution among the set of Pareto optimal solutions for the IGDT-DNRO model, as presented in Section 4.3.

Third Layer (Resilience Assessment): In the third layer (step 13), the resilience index at the uth iteration (i.e., RI_u) is calculated using the ratio of total load value to total load shedding value and expected operation cost value for member u of Ω^{UB}, as discussed in Section 5.1.

Fourth Layer (Optimal CMB Determination): In the fourth layer (steps 14-15), if all values for the budget of uncertainty are evaluated, the optimal budget of uncertainty offering the maximum resilience level (RI^{max}) is identified and reported as the optimal CMB ($CMB = UB^{opt}$). Otherwise, the entire procedure needs to be repeated until evaluating all values of the budget of uncertainty.

6 Case Study and Results

6.1 Test Network and Simulation Data

In this study, the proposed D-DNRO and IGDT-DNRO models have been tested on the modified 33-bus distribution network under different conditions [35]. The MISOCP and SOCP problems have been solved by CPLEXD solver in General Algebraic Modeling System (GAMS) [36] on a laptop computer with 4096 MB of RAM and Intel® core™ i3 processors clocking at 2.3 GHz. The relative optimality criterion for solving the MISOCP/SOCP problems is set to 10^{-3}. Moreover, MATLAB R2008a has been used to calculate the DTR of the tie-line connecting the distribution network to the main grid. The computation time of the proposed resiliency-oriented operational scheduling model outlined in Fig. 1 is only about 11 min on average for all case studies reported in the paper, which shows low computation burden of the proposed model. In order to report applicable and reproducible results, the characteristics of the distribution network, wildlife spread, environmental condition, and DERs (i.e., numbers, capacities, and prices) are chosen in this paper, similar to the previous research works in the literature [14, 37], as further discussed and clarified below.

The 33-bus distribution network includes 32 feeders and 32 load points [35] as depicted in Fig. 2. The locations of MT, WT, PV, and ESS units are shown in this figure. Also, the possible locations for installing rented PMT units are indicated by dotted line in this figure. The active peak load and the maximum apparent power exchange with the upstream network are 15.62 MW and 15.50 MVA, respectively [14]. Also, it is assumed that the network is operated under a balanced condition. The minimum and maximum values of voltage magnitudes are 0.95 and 1.05 p.u., respectively. Moreover, the base apparent power is 100 MVA [38]. The characteristics of the DERs and the ESSs are presented in Table 2 and Table 3, respectively [14, 37]. The profiles of wind and solar generations are given in Fig. 3. The energy exchange price [39], MT/PMT generation cost [28], PMT renting cost [40], MT/PMT startup/shutdown cost and $voll$ [41] are given in Table 4. In this paper, data sets of a summer day are considered to more realistically characterize the propagation of a wildfire. Moreover, the hourly profiles of energy exchange price with the upstream network [39], wind speed [42], wind direction [14], solar radiation [14], ambient temperature [7], and load factor [38] are presented in Table 5. The parameters used for modeling the wildfire [12, 14] and the DTR [11, 43] are presented in Table 6 and Table 7, respectively. In this study, the conductor type of the tie-line connecting the distribution network to the main grid is aluminum conductor steel-reinforced (ACSR)

[43]. It is assumed that a sudden forest wildfire affects the tie-line connecting the distribution network to the main grid (i.e., the tie-line between buses 1 and 2, indicated by red dashed line in Fig. 2) during the scheduling day. In this study, the initial distance between the wildfire and the tie-line is $r_{12,1}^f = 1000$ m.
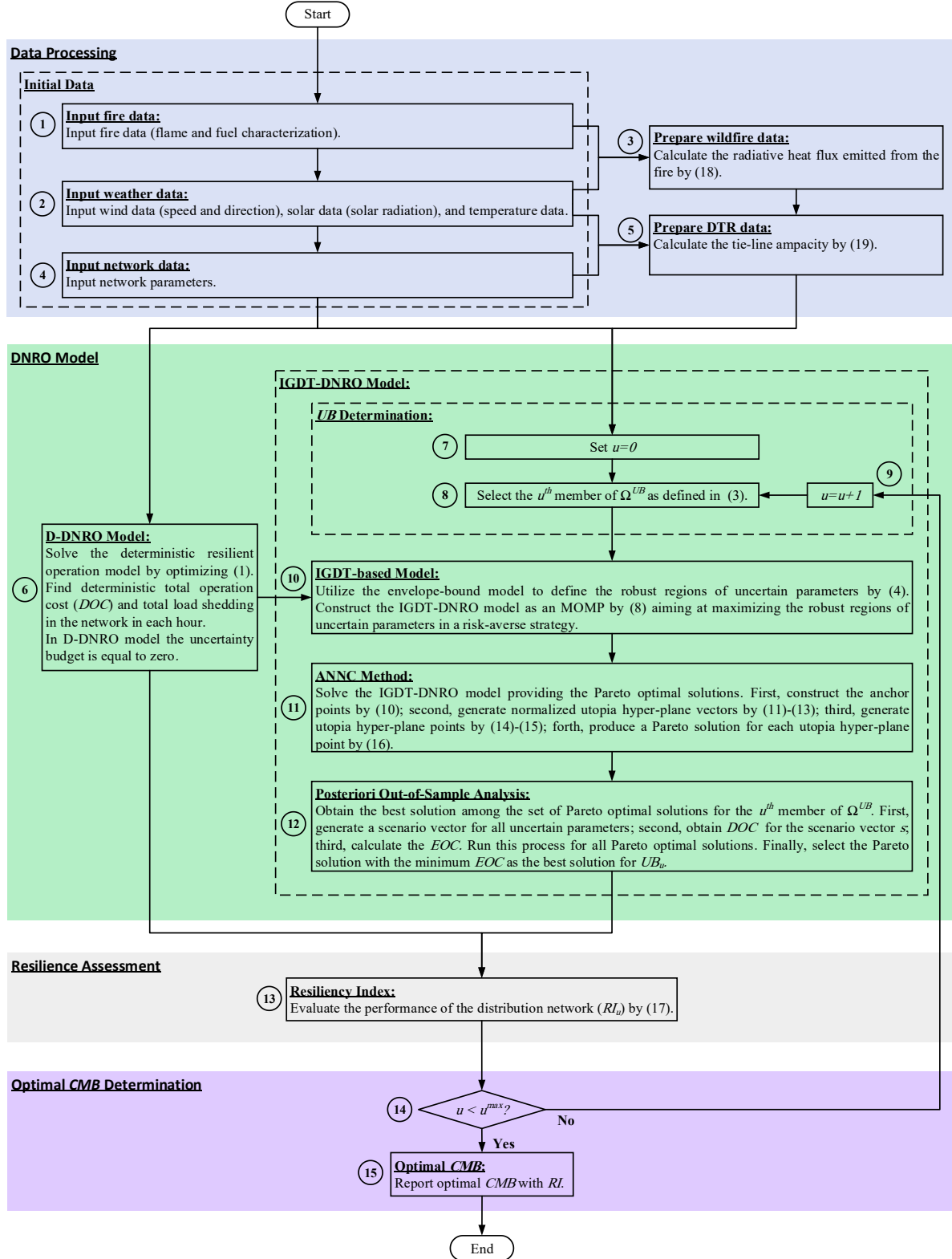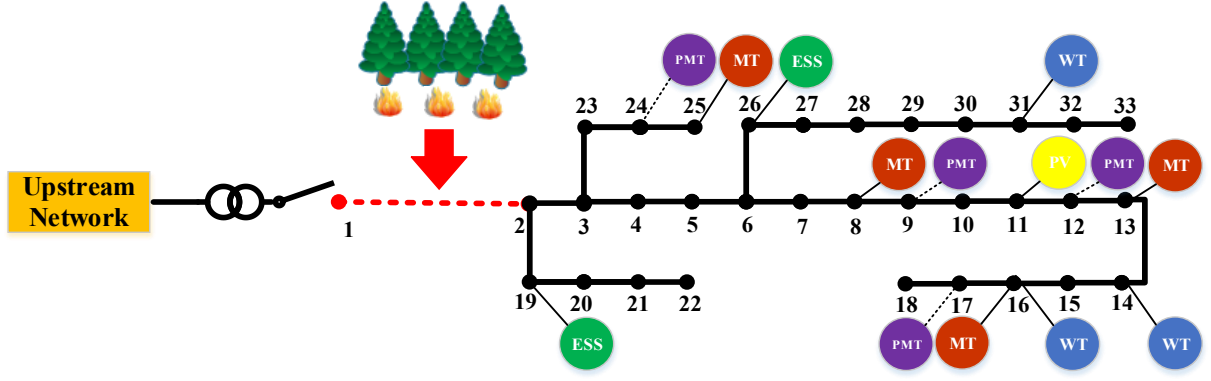

Fig. 1: Proposed framework for DNRO model.

Fig. 2: Single line diagram of the 33-bus distribution network against forest wildfire.

The lost heat by convection, the lost heat by radiation, and the absorbed heat by solar radiation for the tie-line can be calculated as outlined in the first layer of Fig. 1 (i.e., the data processing layer). Its results are illustrated in Fig. 4. It can be observed that the convection heat loss has the major effect on the conductor's heat due to high wind speed values during the scheduling horizon. Moreover, the convection heat loss increases significantly between hours 7:00-8:00 and between hours 17:00-20:00 because of substantial changes in the wind direction (Table 5). Furthermore, the radiative heat loss is negligible due to a very low difference between the ambient and conductor temperatures. Besides, the absorbed heat by solar radiation in the middle of the day is proportional to the amount of solar radiation (Table 5), which is more than other hours of around the clock. In Fig. 5, the distance between the tie-line and the wildfire and the conductor's absorbed heat rate from the wildfire are illustrated. The wildfire approaches the tie-line until hour 21:00, which results in the disconnection of the distribution network from the main grid at this hour. It is observed that the conductor's absorbed heat rate from the wildfire increases significantly when the distance of the wildfire from the tie-line becomes less than 200 m.

Table 2: Location and parameters of DERs [37].

Type of DERs	Bus	$\overline{p_{i,t}}$ (MW)	$\underline{p_{i,t}}$ (MW)	$\overline{q_{i,t}}$ (MVAr)	$\underline{q_{i,t}}$ (MVAr)
MTs	8/13/16/25	3	0.21	2.1	-2.1
PMTs	9/12/17/24	2.5	0.20	2	-2
WTs	14/16/31	0.8	0	-	-
PV	11	0.5	0	-	-
ESSs	19/26	0.5	0	0.3	-0.3

Table 3: Parameters of ESSs [14, 37].

Parameters	Value
$\overline{p^{STC/STD}}$ (MW)	0.5
$\overline{q^{ST}}$ (MVAr)	0.3
$\underline{q^{ST}}$ (MVAr)	-0.3
η_i^{ST}	0.9
$\overline{E_i^{ST}}$ (MWh)	1.5
$\underline{E_i^{ST}}$ (MWh)	0
E_i^{ST-ini} (MWh)	$30\% \times \overline{E_i^{ST}}$

Table 4: Price parameters.

Prices	Value(s)	Refs
c_t^{UP}	Table 5	[39]
c_i^{MT}	72 ($/MWh)	[28]
c_i^{PMT}	4000 ($)	[40]
c_i^{SU}/c_i^{SD}	150/15 ($)	[41]
$voll$	1000 ($/MWh)	

Table 5: Hourly data.

Hour	c_t^{UP} ($/MWh)	w_t (m/s)	$\varphi_{ij,t}^w$ (rad)	φ_t^S (W/m²)	T_t^a (°C)	Load Factor
01:00	15.03	7.11	0.05	0	32.9	0.64
02:00	10.97	7.23	0.17	0	32.1	0.60
03:00	13.51	6.84	0.20	0	30.8	0.58
04:00	15.36	7.08	0.13	0	31.1	0.56
05:00	18.51	6.79	-0.10	0	30.9	0.56
06:00	21.80	6.68	-0.20	30	31.2	0.58
07:00	17.30	6.66	-0.87	130	32.9	0.64
08:00	22.83	6.74	0.30	320	34.3	0.76
09:00	21.84	6.68	0.50	540	35.8	0.87
10:00	27.09	6.92	0.60	730	37.6	0.95
11:00	37.06	6.80	0.40	870	39.0	0.99
12:00	68.95	7.23	0.09	930	39.6	1.00
13:00	65.79	7.08	-0.13	920	39.3	0.99
14:00	66.57	6.86	-0.39	840	39.8	1.00
15:00	65.44	7.22	-0.27	690	39.8	1.00
16:00	79.79	7.56	-0.33	500	40.1	0.97
17:00	115.45	7.65	-0.33	290	39.7	0.96
18:00	110.28	6.90	-0.12	120	39.1	0.96
19:00	96.05	7.11	0.07	20	36.2	0.93
20:00	90.53	7.44	0.20	0	35.6	0.92
21:00	77.38	6.78	0.13	0	34.7	0.92
22:00	70.95	6.75	0.10	0	33.6	0.93
23:00	59.42	6.72	0.13	0	33.1	0.87
24:00	56.68	7.05	0.15	0	33.0	0.72

Table 6: Data used for wildfire modeling [12, 14].

Parameter	Value
τ	1
ε^f	0.5
B	5.6704×10^{-8} $(W/m^2 K^4)$
T^f	1200 (°K)
L^f	10 (m)
γ^f	20 (°)
k^f	0.07 (kg/m^3)
ρ^b	40 (kg/m^3)

Table 7: Data used for DTR modeling.

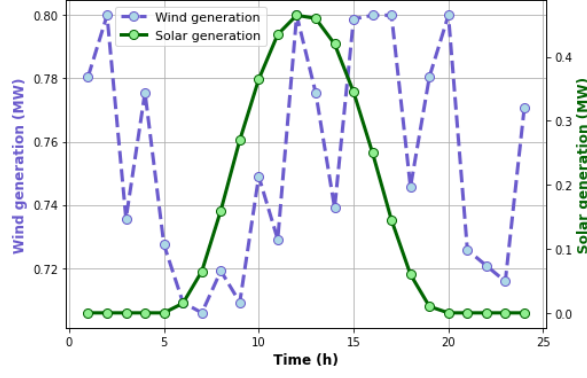| Parameter	Value	Refs
T^{High}	75 (°C)	[43]
T^{Low}	25 (°C)	
$R_{12}(T^{High})$	8.688×10^{-5} (Ω/m)	
$R_{12}(T^{Low})$	7.283×10^{-5} (Ω/m)	
k^a	0.02945 (W/m°C)	
ρ^a	1.029 (kg/m^3)	
μ^a	$2.043 \times 10^{-5}(kg/(m \cdot s))$	
ε	0.5	
D_{12}	28.1 (mm)	
mC^p	534 (J/m°C)	
k_{12}^c	0.5	[11]

Fig. 3: Wind generations at buses 14, 16 & 31 and solar generation at bus 11.
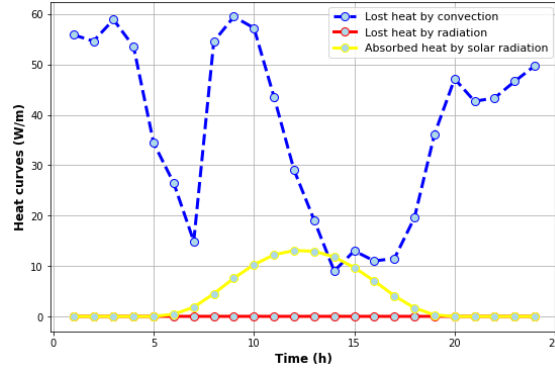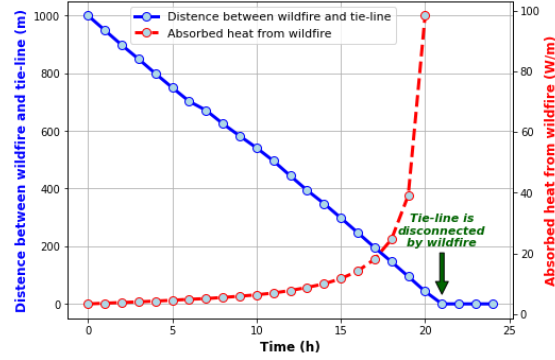

Fig. 4: Heat curves for tie-line.

Fig. 5: Wildfire progressing.

6.2 DNRO Model against Approaching Forest Wildfire

In this section, the D-DNRO and IGDT-DNRO models are utilized to optimize the operation of the distribution network under normal and abnormal conditions. In the IGDT-DNRO model, as a multi-objective optimization problem, five division points are considered on each normalized utopia hyper-plane vector for a specific UB. Each of these vectors connects a pair of four anchor points pertaining to the envelope bounds (i.e., α^{WT}, α^{PV}, α^{D} and α^{ℓ}) of the four robust regions (i.e., $\tilde{p}_{i,t}^{WT}$, $\tilde{p}_{i,t}^{PV}$, $\tilde{p}_{i,t}^{D}$, and $\tilde{\ell}_{12,t}^{DTR}$). Therefore, 35 Pareto optimal solutions corresponding to 35 utopia hyper-plane points are produced using the procedure presented in (15.a)-(15.c). Furthermore, it is assumed that $\alpha^{WT} \leq 1$, $\alpha^{PV} \leq 1$, $\alpha^{D} \leq 0.5$, and $\alpha^{\ell} \leq 1$ to avoid extremely impractical deviations from forecast values of the uncertain parameters; α^{WT}, α^{PV}, and α^{ℓ} cannot be more than 1 because negative values for wind power, solar power and tie-line's DTR are not practical; also, α^{D} cannot be more than 0.5 because more than 50% load forecast error is not reasonable. In the ANNC method, the adjusting factor is considered as $AF \leq 1$ [31], and the importance coefficients are $IC_1 = IC_2 = IC_3 = 0.2$ and $IC_4 = 0.4$. It is noteworthy to mention that a higher weight is considered for the ampacity of the tie-line because the uncertainty of the ampacity of the tie-line has a

higher impact on the resilience of the system as compared to other uncertain parameters due to directly limiting a significant volume of the power exchange with the upstream network.

6.2.1   D-DNRO Model

To evaluate the impact of the wildfire on the optimal operation of the distribution network, two different cases are considered as given below:

Case I: optimal operation of the distribution network by solving the D-DNRO model under the normal condition without any wildfire.

Case II: optimal operation of the distribution network by solving the D-DNRO model under the abnormal condition with the spread of the wildfire.

The ampacity of the tie-line at each hour in both Case I and Case II is depicted in Fig. 6. In Case I, the convection heat loss dominates the solar absorbed heat. Therefore, the ampacity is increased/decreased based on increasing/decreasing variations of the convection heat loss. In Case II, the ampacity is decreased at most of the scheduling hours as the wildfire is approaching the tie-line, and the heat absorbed from the wildfire is increasing. It is noteworthy to mention that the ampacity is increased significantly between hours 7:00-8:00 because the heat lost by convection is increased extensively, as depicted in Fig. 4. The ampacity becomes zero at hour 13:00. In hours 13:00-20:00, the absorbed heat rate (the heat absorbed from the solar irradiance and wildfire spread) is more than the lost heat rate (lost heat from convection and radiation). Finally, the wildfire disconnects the distribution network from the main grid at hour 21:00.

The total active power generation and consumption at each hour in Case I and Case II are given in Fig. 7 and Fig. 8, respectively. According to Fig. 7 and Fig. 8, the total active power generation includes the active power generation of MT/PMT units, the active power received from the upstream network, the active power generation of WT units, the active power generation of PV units, and the active power discharge of ESS units. Also, load shedding is indicated in red in Fig. 7 and Fig. 8. Furthermore, the total active power consumption includes the active load of the distribution network, the active power charge of ESS units, and the active power loss of the distribution network.

The power generation of the PMT units is zero in both Case I and II due to their high renting cost. The power generation of the MT units is increased in Case I and Case II when the price of power purchase from the main grid is higher than the marginal costs of the MT units or when the ampacity of the tie-line is zero. It is observed that the power purchase from the main grid in Case I and Case II is approximately similar during hours 0:00-12:00. In Case I, the ampacity of the tie-line, and consequently, the power received from the main grid is zero at hour 14:00. However, in Case I, during hours 16:00-21:00, the power purchased from the upstream network is approximately zero as the price of power purchase from the main grid is higher than the marginal cost of the MT units in these hours. Finally, during hours 22:00-24:00, the power received from the main grid is increasing because the ampacity of the tie-line and the electricity price of the main grid are increasing and decreasing, respectively. In Case II, during hours 13:00-24:00, the power exchange with the main grid is zero because the tie-line ampacity becomes zero. According to Fig. 7 and Fig. 8, the hourly power generation profiles for WT and PV units are identical in Case I and Case II. Furthermore, the hourly charging and discharging profiles for ESS units are relatively similar in Case I and Case II. It is observed that when the electricity price of the main grid is lower than the marginal cost of the MT units and the tie-line ampacity is not zero, the ESS units are operated in charging mode; otherwise, they are operated in discharging mode as depicted in Fig. 7 and Fig. 8. It is noteworthy to mention that the ampacity of the tie-line changes within a wide range even in Case I without any wildfire as illustrated in Fig. 6. In other words, it is assumed that the distribution network is under tension due to a high temperature in the summer day and specifically at hour 14:00 [7]. Hence, there is load shedding in both Case I and Case II due to inadequate capacity in the distribution network to supply the load. However, the amount of load shedding in Case II is significantly higher than that in Case I as the wildfire in Case II seriously impacts the tie-line ampacity in the second half of the day. Since the distribution network is connected to the upstream grid and the ampacity of tie-line is approximately similar in Case I and Case II until hour 12:00, as depicted in Fig. 6, there is not any load shedding in Case I and Case II until hour 12:00 as shown in Fig. 7 and Fig. 8. After hour 12:00, in Case I, there is load shedding only at hour 14:00 as the tie-line ampacity becomes zero at this hour. On the contrary, after hour 12:00 and until hour 24:00 there is load shedding in Case II as a result of zero tie-line ampacity. There is no load shedding in Case II only at hour 24:00 as a consequence of decreasing the network's load at this hour.

Table 8 reports the total cost, the generation cost, the unit commitment cost, the cost of power purchase from the main network, the load shedding cost, and the total load shedding in Case I and Case II. Since the ampacity of the tie-line is zero in Case II at hours 13:00-24:00, the total cost, generation cost, total load shedding and load shedding cost in Case II are higher than those in Case I, as given in Table 8. Moreover, the cost of power purchase from the main grid in Case I is higher than that in Case II as the ampacity of tie-line in Case I is higher than that in Case II considering more tie-line disconnection hours in Case II. Additionally, it is observed that the unit commitment cost is identical in Case I and Case II as it is cost-effective to run the MT units to supply consumers' demand under the low ampacity of the tie-line and also the low capacity of WT/PV units. The large difference between the total costs in Case I and Case II illustrates the importance of the distribution network resilient operation.
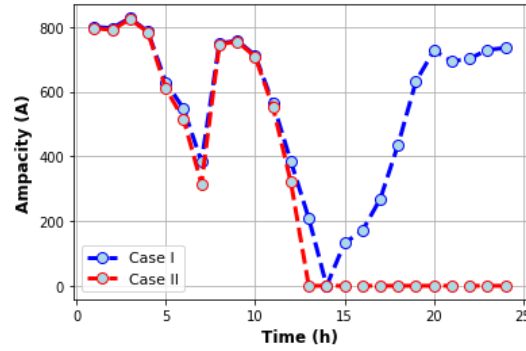

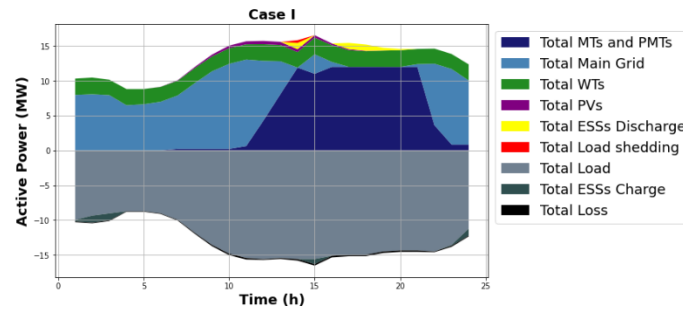**Fig. 6: Tie-line's ampacity in Case I and Case II.**

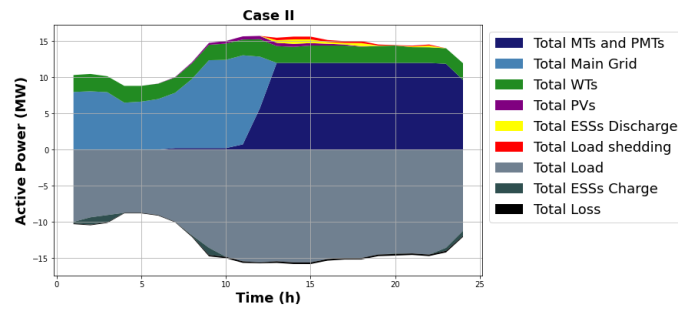**Fig. 7: Total active power at each hour in Case I.**

Fig. 8: Total active power at each hour in Case II.

Table 8: Costs and total load shedding in Case I and Case II.

Case	*DOC* ($)	Generation Cost ($)	Commitment Cost ($)	Power Purchase Cost ($)	Load Shedding Cost ($)	Total Load Shedding (MW)
I	14225.96	8211.13	600.00	5018.51	396.32	0.40
II	18266.42	14106.02	600.00	1198.07	2362.33	2.36

6.2.2 IGDT-DNRO Model

To evaluate the proposed IGDT-DNRO model, Case III is considered, which is similar to Case II. The proposed IGDT-DNRO model is solved for various values of UB where 35 different Pareto optimal solutions are obtained for every UB value. Although the upper bound of the operation costs for all Pareto optimal solutions are identical for a specific UB value, their envelope bounds are different. Hence, a posteriori out-of-sample analysis, including five scenarios with different wildfire severities for the ampacity of the tie-line, is utilized to obtain the most resilient operation plan, owning the maximum RI value, among the 35 Pareto optimal solutions of a specific UB. The ampacity of the tie-line inversely affects the load shedding. In other words, the lower/higher the ampacity of the tie-line, the higher/lower the load shedding, and consequently, the lower/higher the resilience index. In addition, wildfire severity directly impacts line ampacities because the wildfire heat can be transferred via radiation to lines and increase their conductors' temperatures [14]. Fig. 5 and Fig. 6 show how the absorbed heat from wildfire can decrease the tie-line ampacity and even disconnect the tie-line. For these reasons, different tie-line ampacities are used in this paper to define wildfire severity levels. Therefore, in these five wildfire scenarios, denoted as low, medium-low, medium, medium-high, and high, the tie-line's ampacity is considered as 1.20, 1.10, 1.00, 0.90, and 0.80 times of the tie-line ampacity in Case II in Fig. 6, respectively [10]. The best resilient plans for $UB = 0.00$ to $UB = 2.00$ are given in Table 9.

Table 9: Costs, PMT buses, robust regions, and resiliency index in Case III.

UB	ROC ($)	Generation Cost ($)	Commitment Cost ($)	Power Purchase Cost ($)	Load Shedding Cost ($)	PMT buses	EOC ($)	α^{WT}	α^{PV}	α^D	α^ℓ	$\frac{TL_u}{1+TLS_u} \times 10^{-3}$	$RI_u \times 10^{-3}$
0.00	18266.42	14106.02	600.00	1198.07	2362.33	-	18826.58	0.00	0.00	0.00	0.00	92.54	4.92
0.40	25572.99	18234.50	4750.00	1156.27	1432.22	9	24310.92	0.85	1.00	0.02	0.10	129.79	5.34
0.80	32879.56	22189.58	8900.00	1052.90	737.08	9/17	30956.69	1.00	1.00	0.15	0.25	205.42	6.64
1.20	40186.12	26276.00	13050.00	860.11	0.01	9/17/24	37660.67	1.00	1.00	0.30	0.50	404.04	10.73
1.60	47492.69	29677.27	17200.00	615.40	0.02	9/12/17/24	44941.39	1.00	1.00	0.42	0.74	440.42	9.80
2.00	54799.26	32845.93	17200.00	103.42	4649.91	9/12/17/24	55842.92	1.00	1.00	0.50	0.99	82.30	1.47

According to Table 9, it can be concluded that:

- The value of ROC is increased by increasing UB from 0.00 to 2.00 where ROC refers to the worst-case total cost. Note that ROC can adopt higher values by increasing UB as $ROC \leq (1 + UB) \cdot DOC$. Moreover, more immunizations against different realizations of uncertain parameters are provided by increasing UB due to obtaining higher values for envelope bounds offering wider robust regions. In other words, by increasing UB, higher robustness is provided at the expense of higher ROC. Similarly, EOC increases by increasing UB. It is worthwhile to note that the results of the proposed IGDT-DNRO model for $UB = 0.00$ in Case III are the same results of the proposed D-DNRO model in Case II, since $ROC = (1 + UB) \cdot DOC = (1 + 0) \cdot DOC = DOC$.

- The generation and commitment costs of MT/PMT units are increased by increasing UB due to two reasons. First, α^{WT}, α^{PV}, and α^ℓ are increased, and consequently, the wind and solar power generations and power purchased from the main grid are decreased. Second, α^D is increased, and therefore, the load of the distribution network is increased. Thus, for compensating the decreased renewable generation/power purchase and the increased load, the power generations of MT/PMT units, and thus their associated generation and commitment costs, are increased.

- The cost of power purchased from the upstream network is decreased by increasing UB, since α^ℓ is increased, and thus, the ampacity of the tie-line is decreased.

- By increasing UB, the load shedding cost is first decreased (from $UB = 0.00$ to $UB = 1.20$), then is remained approximately constant (from $UB = 1.20$ to $UB = 1.60$), and subsequently is increased (from $UB = 1.60$ to $UB = 2.00$). By increasing UB, although load may be increased due to increasing α^D, the IGDT-DNRO model can rent and employ PMT units to supply the additional load and decrease the load shedding. Thus, by increasing UB from 0.00 to 1.60, as shown in Table 9, the rented PMT units are increased and thus the load shedding cost decreases to about zero (from $UB = 0.00$ to $UB = 1.20$) and remains about zero (from $UB = 1.20$ to $UB = 1.60$). However, by further increasing UB from 1.60, the load shedding cost increases as there is no further PMT unit to be rented.

- While α^{WT}, α^{PV}, α^D, and α^ℓ increase by increasing UB, they have different rates of increase in Table 9. It is due to the fact that the capacity of WT and PV units are significantly lower than the distribution network load and the tie-line rating in this test system. Thus, the increase rates of α^{WT} and α^{PV} are higher than the

increase rates of α^D and α^ℓ as a specific change in terms of MW leads to a higher percentage change in the wind and solar powers compared to the percentage change in the load and tie-line rating. For instance, Table 9 shows that by increasing UB from 0.00 to 0.40, α^{WT} and α^{PV} increase by 85% and 100%, while α^D and α^ℓ increase by 2% and 10%. In addition, in the numerical experiment of Table 9, the maximum value of UB is selected 2 as in this UB value all envelope bounds approximately reach their maximum limits.

- If only the loss of load is considered as the resiliency index, $UB = 1.60$, indicated in yellow color in Table 9, leads to the most resilient operation plan as it has the highest ratio of the total load to the total load shedding (or equivalently, the minimum ratio of the total load shedding to the total load). However, using the proposed resiliency index, which concurrently considers the impacts of both expected operation cost and load shedding ratio, $UB = 1.20$, indicated in green color in Table 9, results in the most resilient operation plan. Thus, $UB^{opt} = CMB = 1.20$ in this test case. Also, it is seen that the resiliency index of the most resilient operation plan (i.e., $RI^{max} = RI_{1.2} = 10.73$) is significantly higher than the resiliency index of the deterministic model operation plan (i.e., $RI_0 = 4.92$), which further indicates the effectiveness of the proposed IGDT-DNRO model.

- According to the discussion of the previous point, using the proposed a posteriori out-of-sample analysis, the most resilient operation plan can be determined based on the preferences of the distribution system operator.

To further investigate the performance of the IGDT-DNRO model with the most resilient operational schedule (i.e., Case III with $UB^{opt} = 1.20$ in Table 9) as compared to the D-DNRO model (i.e., Case II with $UB = 0.00$ in Table 8), the total active power generation and consumption at each hour in Case III are presented in Fig. 9. Based on Fig. 8 and Fig. 9, it can be observed that:

- The total load of the network in Case III is increased by about 30% as compared to Case II because of a non-zero value for the robust region of the load demand in the IGDT-DNRO model, i.e., $\alpha^D = 0.30$.

- The power generation of MT/PMT units in Case III is significantly higher than that in Case II. In contrast to Case II, the power generation of the PMT units is non-zero in Case III because of the increased load demand of the network and the decreased ampacity of the tie-line connecting the distribution network to the main grid. However, similar to Case II, the power generation of the MT/PMT units in Case III is increased when the price of power purchased from the main grid is higher than the marginal costs of the MT/PMT units or when the ampacity of the tie-line is zero.

- The power purchase from the main grid in Case III is significantly decreased as compared to Case II because of the non-zero value of the robust region of the tie-line connecting the distribution network to the main grid during hours 0:00-12:00, i.e., $\alpha^\ell = 0.50$.

- In contrast to Case II, the power generation of WT and PV units in Case III is zero because of non-zero values for their robust regions, i.e., $\alpha^{WT} = 1.00$ and $\alpha^{PV} = 1.00$.

- The charging and discharging of ESS units in Case III are less than in Case II. The main reasons are: (i) the ampacity of the tie-line, and consequently, the power purchased from the main grid is decreased during hours 0:00-12:00, and (ii) the total load of the network is increased by about 30%, and consequently, the MT/PMT units are in operation during these hours despite the electricity price of the upstream network is lower than the marginal cost of the MT/PMT units.

- Despite the total load of the network in Case III is higher than in Case II, the load shedding in Case III is less than that in Case II. In other words, the load shedding in Case III is about zero because of utilizing/renting MT/PMT units.
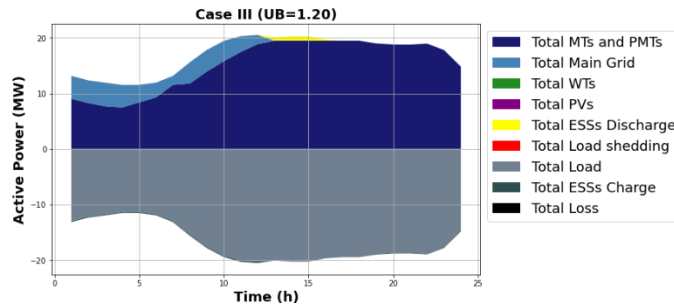

Fig. 9: Total active power at each hour in Case III ($UB^{opt} = 1.20$).

In addition to comparing the total active power generation and consumption at each hour for both the D-DNRO and IGDT-DNRO models in Case II (Fig. 8) and Case III (Fig. 9), respectively, the nodal load shedding and the nodal voltage profile for two selected buses (i.e., 30 and 32) in Case II and Case III for $UB^{opt} = 1.20$ are depicted in Fig. 10 and Fig. 11 to further compare the performance of the D-DNRO and IGDT-DNRO models. While the amount of load shedding at bus 30 (blue color) and bus 32 (gray color) is non-zero for several hours in Case II (i.e., 13:00-22:00), as shown in Fig. 10, there is no load shedding at those buses in Case III for $UB^{opt} = 1.20$ because the power generation of MT/PMT units in Case III is substantially higher than that in Case II. Furthermore, as depicted in Fig. 11, the nodal voltage profiles at buses 30 and 32 in Case III for $UB^{opt} = 1.20$ (blue and red solid lines, respectively) are higher than those in Case II (blue and red dashed lines, respectively) because there is more local generation in Case III as compared to Case II.

In summary, it can be concluded that the main benefits of the IGDT-DNRO model with the most resilient operational schedule ($UB^{opt} = 1.20$) are related to a significantly lower amount of load shedding as compared to the D-DNRO model while the operation conditions in Case III are worse than those in Case II, i.e., the power generation of WT and PV units are zero, the total load of the network is increased by 30%, and the ampacity of the tie-line connecting the distribution network to the main grid is decreased by 50% in Case III as compared to Case II. Furthermore, the higher voltage profiles in Case III ($UB^{opt} = 1.20$) as compared to those in Case II are the other evidence for the superiority of the proposed IGDT-DNRO model over the D-DNRO model.
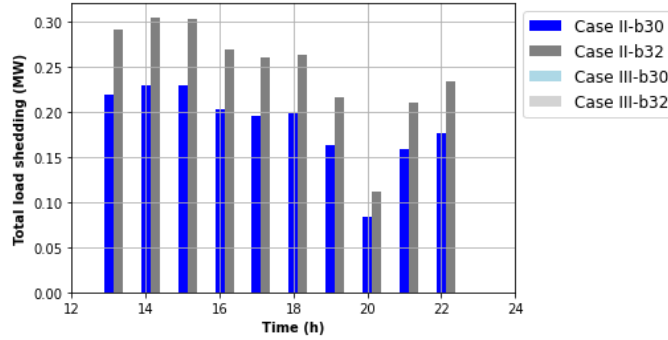

Fig. 10: The amount of load shedding for buses 30 and 32 in Case II and Case III ($UB^{opt} = 1.20$).
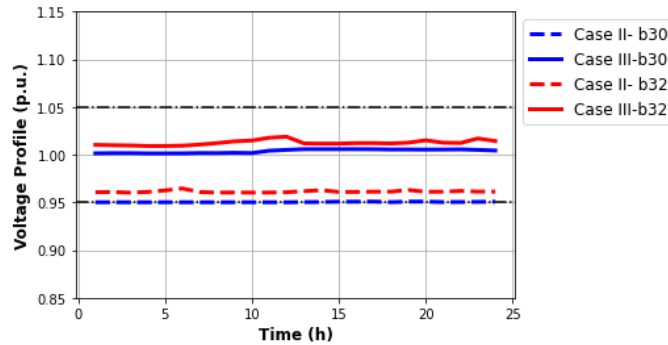

Fig. 11: The voltage profiles for buses 30 and 32 in Case II and Case III ($UB^{opt} = 1.20$).

7   Conclusion

This paper presents a robust model (IGDT-DNRO) for enhancing the resilience of distribution network operation under the spread of a wildfire as a disastrous event. The influence of the fire heat on the performance of the tie-line connecting the distribution network to the main grid is modeled. The resilient operation is achieved by maximizing the robust region of each uncertain parameter for a particular UB value. Therefore, the proposed IGDT-DNRO model is presented as a multi-objective optimization problem and solved by the ANNC approach. A posteriori out-of-sample analysis is utilized to obtain the most resilient operation plan among a set of Pareto

optimal solutions generated by the ANNC approach. The proposed IGDT-DNRO model and its solution method have been tested on the modified 33-bus distribution system. The results demonstrate that the proposed IGDT-DNRO model can enhance the operational resiliency against wildfire by finding robust solutions with different immunization levels against the uncertainty sources. Furthermore, the crisis management budget, as the optimum value of the uncertainty budget, has been obtained by maximizing the distribution network resiliency index.

In summary, it can be concluded:

- The proposed RI index can evaluate the actual performance of the network during the spread of the wildfire.
- The proposed IGDT-DNRO model can determine optimum CMB with maximum RI by reducing the nodal load shedding and enhancing the nodal voltage profiles under the worst-case condition.
- Using a posteriori out-of-sample analysis, the most resilient operation plan can be obtained based on the preference of the distribution system operator.
- The proposed D-DNRO and IGDT-DNRO models enforce a reasonable computational burden for resilient operational scheduling in distribution networks, which makes these models appropriate for practical applications.

Future research will be focused on extending the proposed resiliency-oriented scheduling framework to (1) include uncertainties of wind speed and wind direction explicitly and (2) incorporate the overall system DTR level in the resiliency index under different loading conditions.

8   Appendix

In this section, the mathematical models with technical constraints for the wildfire spread and the dynamic thermal rating of the line connecting the distribution network to the upstream network are presented in Sections 8.1 and 8.2, respectively.

8.1   Wildfire Formulation

The mathematical formulation of the wildfire spread as a function of different environmental parameters is given below [44]:

$$V_t^f = \frac{k^f (1 + w_t)}{\rho^b} \quad \forall t \tag{18.a}$$

$$r_{ij,t}^f = r_{ij,t-1}^f - \left(V_t^f \cdot \Delta t \cdot 3600 \cdot \cos \varphi_{ij,t}^w \right) \quad \forall (i,j), \forall t \tag{18.b}$$

where (18.a) represents the speed of fire spread and (18.b) denotes the distance of fire from the line.

$$\delta_{ij,t}^f = \tan^{-1} \left(\frac{L^f \cdot \cos \gamma^f}{r_{ij,t}^f - (L^f \sin \gamma^f)} \right) \quad \forall (i,j), \forall t \tag{18.c}$$

$$\varphi_{ij,t}^f = \frac{\tau \cdot \varepsilon^f \cdot B \cdot T^{f^4}}{2} \sin \delta_{ij,t}^f \quad \forall (i,j), \forall t \tag{18.d}$$

Also, (18.c) denotes the angle of view between the flame and the conductor and (18.d) represents the radiative heat flux emitted from the fire. It is worthwhile to mention that the simplified heat flux model in [44] is used in this paper to characterize the wildfire spread. In summary, $\varphi_{ij,t}^f$ in (18.d) can be calculated by finding V_t^f in (18.a), $r_{ij,t}^f$ in (18.b), and $\delta_{ij,t}^f$ in (18.c) at each hour of the scheduling horizon one after another. In the sequel, $\varphi_{ij,t}^f$ is used to calculate the amount of absorbed heat corresponding to the radiative heat flux emitted from the fire (i.e., $q_{ij,t}^f$), and consequently, to obtain the amount of DTR at each hour of the scheduling horizon.

8.2   Dynamic Thermal Rating Formulation

The mathematical formulation of the DTR of the line connecting the distribution network to the upstream network during the spread of the wildfire can be described by the following equations [14, 43]:

$$K_{ij,t}^{Angle} = 1.194 - \cos\left(\varphi_{ij,t}^w\right) + 0.194 \cos\left(2\varphi_{ij,t}^w\right) + 0.368 \sin\left(2\varphi_{ij,t}^w\right) \quad \forall (i,j), \forall t \tag{19.a}$$

$$N_{ij,t}^{Re} = \frac{D_{ij} \cdot \rho^a \cdot w_t}{\mu^a} \quad \forall (i,j), \forall t \tag{19.b}$$

The wind direction factor and the Reynolds number for the forced convection are presented by (19.a) and (19.b), respectively [43].

$$q_{ij,t}^c = K_{ij,t}^{Angle} \cdot 0.754 \cdot \left(N_{ij,t}^{Re}\right)^{0.6} \cdot k^a \cdot \left(T_{ij,t} - T_t^a\right) \quad \forall(i,j), \forall t \tag{19.c}$$

$$q_{ij,t}^r = 17.8 D_{ij} \cdot \varepsilon \cdot \left[\left(\frac{T_{ij,t} + 273}{100}\right)^4 - \left(\frac{T_t^a + 273}{100}\right)^4\right] \quad \forall(i,j), \forall t \tag{19.d}$$

The amount of lost heat caused by convection and radiation are described by (19.c) and (19.d), respectively. Note that the natural convention is excluded for non-zero wind speeds in this paper, and only the forced convention is included for high wind speeds in (19.c).

$$q_{ij,t}^s = k_{ij}^c \cdot D_{ij} \cdot \varphi_{ij,t}^s \quad \forall(i,j), \forall t \tag{19.e}$$

$$q_{ij,t}^f = D_{ij} \cdot \varphi_{ij,t}^f \quad \forall(i,j), \forall t \tag{19.f}$$

The amount of absorbed heat caused by solar radiation and radiative heat flux emitted from the fire are calculated by (19.e) and (19.f), respectively. It is noteworthy to mention that $\varphi_{ij,t}^f$ in (19.f) can be calculated by equation (18.d), as discussed in Section 8.1.

$$R_{ij,t}\left(T_{ij,t}\right) = \left[\frac{R_{ij}(T^{High}) - R_{ij}(T^{Low})}{T^{High} - T^{Low}}\right] \cdot \left(T_{ij,t} - T^{Low}\right) + R_{ij}(T^{Low}) \quad \forall(i,j), \forall t \tag{19.g}$$

$$I_{ij,t}^{DTR} = \sqrt{\frac{q_{ij,t}^c + q_{ij,t}^r - q_{ij,t}^s - q_{ij,t}^f}{R_{ij,t}\left(T_{ij,t}\right)}} \quad \forall(i,j), \forall t \tag{19.h}$$

$$T_{ij,t+1} - T_{ij,t} = \frac{\Delta t \times 3600}{mC^p}\left[R_{ij,t}\left(T_{ij,t}\right) \cdot I_{ij,t}^2 + q_{ij,t}^s + q_{ij,t}^f - q_{ij,t}^c - q_{ij,t}^r\right] \quad \forall(i,j), \forall t \tag{19.i}$$

The resistance of the conductor as a function of the temperature is given by (19.g). The maximum DTR of the tie-line at each hour is expressed by (19.h). It is worthwhile to mention that the distribution network will be operated in islanded mode if the maximum DTR of the tie-line is equal to zero. Also, the maximum DTR of the tie-line can be calculated after obtaining the values of $q_{ij,t}^c$, $q_{ij,t}^r$, $q_{ij,t}^s$, $q_{ij,t}^f$, and $R_{ij,t}\left(T_{ij,t}\right)$ by equations (19.a)-(19.c), (19.d), (19.e), (19.f), and (19.g), respectively. Since the conductor temperature is needed to calculate the maximum DTR of the tie-line for the next hour of the study period, it can be obtained by (19.i) [14].

References

[1] Abedi A, Gaudard L, Romerio F. Review of major approaches to analyze vulnerability in power system. Reliability Engineering & System Safety. 2019;183:153-72.

[2] Izadi M, Hosseinian SH, Dehghan S, Fakharian A, Amjady N. A critical review on definitions, indices, and uncertainty characterization in resiliency-oriented operation of power systems. International Transactions on Electrical Energy Systems. 2021;31:e12680.

[3] Jufri FH, Widiputra V, Jung J. State-of-the-art review on power grid resilience to extreme weather events: Definitions, frameworks, quantitative assessment methodologies, and enhancement strategies. Applied Energy. 2019;239:1049-65.

[4] Panteli M, Mancarella P. The grid: Stronger, bigger, smarter?: Presenting a conceptual framework of power system resilience. IEEE Power and Energy Magazine. 2015;13:58-66.

[5] Panteli M, Trakas DN, Mancarella P, Hatziargyriou ND. Power Systems Resilience Assessment: Hardening and Smart Operational Enhancement Strategies. Proceedings of the IEEE. 2017;105:1202-13.

[6] Zhang P, Ban Y, Nascetti A. Learning U-Net without forgetting for near real-time wildfire monitoring by the fusion of SAR and optical time series. Remote Sensing of Environment. 2021;261:112467.

[7] Guo Y, Chen R, Shi J, Wan J, Yi H, Zhong J. Determination of the power transmission line ageing failure probability due to the impact of forest fire. IET Generation, Transmission & Distribution. 2018;12:3812-9.

[8] Bagchi A, Sprintson A, Singh C. Modeling the impact of fire spread on an electrical distribution network. Electric Power Systems Research. 2013;100:15-24.

[9] Bagchi A, Sprintson A, Guikema S, Bristow E, Brumbelow K. Modeling performance of interdependent power and water networks during urban fire events. 2010 48th Annual Allerton Conference on Communication, Control, and Computing (Allerton). Monticello, IL, USA: IEEE; 2010. p. 1637-44.

[10] Ansari B, Mohagheghi S. Optimal energy dispatch of the power distribution network during the course of a progressing wildfire. International Transactions on Electrical Energy Systems. 2015;25:3422-38.

[11] Mohagheghi S, Rebennack S. Optimal resilient power grid operation during the course of a progressing wildfire. International Journal of Electrical Power & Energy Systems. 2015;73:843-52.

[12] Choobineh M, Ansari B, Mohagheghi S. Vulnerability assessment of the power grid against progressing wildfires. Fire Safety Journal. 2015;73:20-8.

[13] Choobineh M, Mohagheghi S. Power grid vulnerability assessment against wildfires using probabilistic progression estimation model. 2016 IEEE Power and Energy Society General Meeting (PESGM). Boston, MA, USA: IEEE; 2016. p. 1-5.

[14] Trakas DN, Hatziargyriou ND. Optimal distribution system operation for enhancing resilience against wildfires. IEEE Transactions on Power Systems. 2017;33:2260-71.

[15] Amjady N, Attarha A, Dehghan S, Conejo AJ. Adaptive robust expansion planning for a distribution network with DERs. IEEE Transactions on Power Systems. 2017;33:1698-715.

[16] Ehsan A, Yang Q. State-of-the-art techniques for modelling of uncertainties in active distribution network planning: A review. Applied energy. 2019;239:1509-23.

[17] Dehghan S, Kazemi A, Amjady N. Multi-objective robust transmission expansion planning using information-gap decision theory and augmented ε-constraint method. IET Generation, Transmission & Distribution. 2014;8:828-40.

[18] Yazdaninejad M, Amjady N, Dehghan S. VPP self-scheduling strategy using multi-horizon IGDT, enhanced normalized normal constraint, and bi-directional decision-making approach. IEEE Transactions on Smart Grid. 2019;11:3632-45.

[19] Dai X, Wang Y, Yang S, Zhang K. IGDT-based economic dispatch considering the uncertainty of wind and demand response. IET Renewable Power Generation. 2019;13:856-66.

[20] Soroudi A, Maghouli P, Keane A. Resiliency oriented integration of DSRs in transmission networks. IET Generation, Transmission & Distribution. 2017;11:2013-22.

[21] Aldarajee AH, Hosseinian SH, Vahidi B. A secure tri-level planner-disaster-risk-averse replanner model for enhancing the resilience of energy systems. Energy. 2020;204:117916.

[22] Aldarajee AH, Hosseinian SH, Vahidi B, Dehghan S. A coordinated planner-disaster-risk-averse-planner investment model for enhancing the resilience of integrated electric power and natural gas networks. International Journal of Electrical Power & Energy Systems. 2020;119:105948.

[23] Li H, Zou Z, Li H, Chen Y, Fu C. Thermal performance of a microchannel primary surface recuperator for portable microturbine generators: Design and experimental study. Applied Thermal Engineering. 2022:118103.

[24] Amjady N, Dehghan S, Attarha A, Conejo AJ. Adaptive robust network-constrained AC unit commitment. IEEE transactions on power systems. 2016;32:672-83.

[25] Farivar M, Low SH. Branch flow model: Relaxations and convexification—Part I. IEEE Transactions on Power Systems. 2013;28:2554-64.

[26] Dehghan S, Amjady N. Robust transmission and energy storage expansion planning in wind farm-integrated power systems considering transmission switching. IEEE Transactions on Sustainable Energy. 2016;7:765-74.

[27] Xu G, Qiao C, Wang X, Wu H, Yang S, Ma L, et al. A Multi-layer Optimized Configuration Method for Energy Storage Device and Compensation Device on Long-Chain Power Distribution Line. 2021 8th International Conference on Electrical and Electronics Engineering (ICEEE): IEEE; 2021. p. 150-4.

[28] Ahmadigorji M, Amjady N, Dehghan S. A robust model for multiyear distribution network reinforcement planning based on information-gap decision theory. IEEE Transactions on Power Systems. 2017;33:1339-51.

[29] Ben-Haim Y. Info-gap decision theory: decisions under severe uncertainty. Amsterdam, Netherlands: Elsevier; 2006.

[30] Messac A, Ismail-Yahaya A, Mattson CA. The normalized normal constraint method for generating the Pareto frontier. Structural and multidisciplinary optimization. 2003;25:86-98.

[31] Bagheri B, Amjady N. Stochastic multiobjective generation maintenance scheduling using augmented normalized normal constraint method and stochastic decision maker. International Transactions on Electrical Energy Systems. 2019;29:e2722.

[32] Hossain E, Roy S, Mohammad N, Nawar N, Dipta DR. Metrics and enhancement strategies for grid resilience and reliability during natural disasters. Applied Energy. 2021;290:116709.

[33] Labaka L, Hernantes J, Sarriegi JM. Resilience framework for critical infrastructures: An empirical study in a nuclear plant. Reliability Engineering & System Safety. 2015;141:92-105.

[34] Kumar BK, Singh S, Srivastava S. A decentralized nonlinear feedback controller with prescribed degree of stability for damping power system oscillations. Electric power systems research. 2007;77:204-11.

[35] Baran M, Wu FF. Optimal sizing of capacitors placed on a radial distribution system. IEEE Transactions on power Delivery. 1989;4:735-43.

[36] GAMS Generalized Algebraic Modelling System.

[37] Gholami A, Shekari T, Aminifar F, Shahidehpour M. Microgrid Scheduling With Uncertainty: The Quest for Resilience. IEEE Transactions on Smart Grid. 2016;7:2849-58.

[38] Atwa Y, El-Saadany E, Salama M, Seethapathy R. Optimal renewable resources mix for distribution system energy loss minimization. IEEE Transactions on Power Systems. 2009;25:360-70.

[39] Khodaei A. Microgrid optimal scheduling with multi-period islanding constraints. IEEE Transactions on Power Systems. 2013;29:1383-92.

[40] HOMER Pro.

[41] Farzin H, Fotuhi-Firuzabad M, Moeini-Aghtaie M. Stochastic energy management of microgrids during unscheduled islanding period. IEEE Transactions on Industrial Informatics. 2016;13:1079-87.

[42] Papaioannou D, Papadimitriou C, Dimeas A, Zountouridou E, Kiokes G, Hatziargyriou N. Optimization & sensitivity analysis of microgrids using HOMER software-A case study. MedPower 2014. Athens, Greece: IET; 2014.

[43] Muratori B. IEEE standard for calculating the current-temperature relationship of bare overhead conductors. IEEE Standard. 2013:738-2012.

[44] Rossi J-L, Simeoni A, Moretti B, Leroy-Cancellieri V. An analytical model based on radiative heating for the determination of safety distances for wildland fires. Fire Safety Journal. 2011;46:520-7.